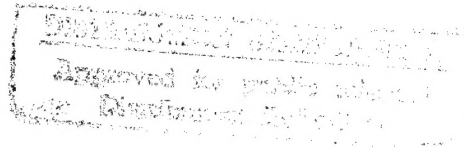


NASA CONTRACTOR REPORT

NASA CR-134691

NASA CR-134691



19960206 137

INVESTIGATION OF FATIGUE STRENGTH OF MULTILAYER ADVANCED FIBER COMPOSITES

by H. R. Thornton and T. J. Kozik

Texas A&M University
Department of Mechanical Engineering
College Station, Texas

prepared for

NATIONAL AERONAUTICS AND SPACE ADMINISTRATION

NASA Lewis Research Center
Grant No. NGR 44-001-149

PLASTEC

22515

1. Report No. NASA CR-134691		2. Government Accession No.		3. Recipient's Catalog No.	
4. Title and Subtitle Investigation of Fatigue Strength of Multilayer Advanced Fiber Composites				5. Report Date September 1974	
				6. Performing Organization Code	
7. Author(s) H. R. Thornton and T. J. Kozik				8. Performing Organization Report No. TEES-2992-74-002	
9. Performing Organization Name and Address Texas A&M University Department of Mechanical Engineering College Station, TX 77840				10. Work Unit No.	
				11. Contract or Grant No. NGR 44-001-149	
12. Sponsoring Agency Name and Address National Aeronautics and Space Administration Washington, DC 20546				13. Type of Report and Period Covered Final Report	
				14. Sponsoring Agency Code	
15. Supplementary Notes Project Manager, C. C. Chamis Materials and Structures Division NASA-Lewis Research Center Cleveland, OH 44135					
16. Abstract <p>The analytical characterization of a multilayer fiber composite plate (without hole) was accomplished for both static and dynamic loading conditions using the finite difference technique. Thornel 300/5208 composites with and without holes were subjected to static and tensile fatigue testing. Five (5) fiber orientations were submitted to test. Tensile fatigue testing also included three (3) loading conditions and two (2) frequencies. The low-cycle test specimens demonstrated a shorter tensile fatigue life than the high-cycle test specimens.</p> <p>Failure surfaces demonstrated effect of testing conditions. Secondary failure mechanisms, such as: delamination, fiber breakage, and edge fiber delamination were present in $[0/+45/0]_s$ and $[0/+60/0]_s$ specimens. Longitudinal delamination between plies also occurred in these specimens.</p>					
17. Key Words (Suggested by Author(s)) Fatigue strength Fiber composites Failure mechanism			18. Distribution Statement Unclassified Unlimited		
19. Security Classif. (of this report) Unclassified		20. Security Classif. (of this page) Unclassified		21. No. of Pages 71	
				22. Price* \$3.00	

* For sale by the National Technical Information Service, Springfield, Virginia 22151

FOREWARD

This final report is submitted in fulfillment of Grant No. NGR 44-001-149. This effort was accomplished between June 15, 1973 and July 31, 1974.

The research was accomplished within the Department of Mechanical Engineering, Texas A&M University. Graduate students making contributions were Steven Albright, Clarence Ko, and Steven Sun.

The graphite-epoxy composite test specimens used in the investigation were furnished by Dr. G. P. Sendeckyi of the Advanced Composites Branch, Air Force Flight Dynamics Laboratory (AFFDL), Wright-Patterson Air Force Base, Ohio. Dr. G. P. Sendeckyj was responsible for technical input concerning composite fracture mechanics.

The NASA Project Officer for this program was Dr. C. C. Chamis of the Materials and Structures Division, Lewis Research Center.

TABLE OF CONTENTS

	Page
I. INTRODUCTION	1
1. Theory of Failure	3
2. Fracture Mechanics Applied to Composites	4
3. Fatigue	5
II. TECHNICAL APPROACH	7
III. ANALYTICAL CHARACTERIZATION	10
1. Nomenclature	11
2. Generalized Anisotropic Plate Analysis	12
2.1 Elastic Constants	12
2.2 Governing Equations for a Laminate with Hole and Symmetrically Loaded	14
3. Dynamic Plate Model-No Hole	16
4. Static and Dynamic Plate Model with Hole	41
IV. EXPERIMENTAL DATA	43
1. Graphite-Epoxy Composite	44
2. Static Test Results	45
3. Tensile Fatigue Results	45
4. Test Specimen Failure	57
V. DISCUSSION	65
VI. CONCLUSIONS	68
REFERENCES	69

LIST OF FIGURES

<u>FIGURE</u>		<u>PAGE</u>
1	Composite Test Specimen Configuration	8
2	Strain Energy Density Field of Unidirectional Graphite-Epoxy Composite under 10,000 μ -inch Displacement at $x = 2$ -inch.	21
3	Strain Energy Density Field of [0/+15/0] Graphite-Epoxy Composite under 10,000 μ -inch Displacement at $x = 2$ -inch.	22
4	Strain Energy Density Field of [0/+30/0] Graphite-Epoxy Composite under 10,000 μ -inch Displacement at $x = 2$ -inch.	23
5	Strain Energy Density Field of [0/+45/0] Graphite-Epoxy Composite under 10,000 μ -inch Displacement at $x = 2$ -inch.	24
6	Strain Energy Density Field of [0/+60/0] Graphite-Epoxy Composite under 10,000 μ -inch Displacement at $x = 2$ -inch.	25
7	Strain Energy Density Field of Unidirectional Graphite-Epoxy Composite under 10,500 μ -inch Displacement at $x = 2$ -inch.	26
8	Strain Energy Density Field of Unidirectional Graphite-Epoxy Composite under 10,000 μ -inch Displacement at $x = 2$ -inch.	27
9	Strain Energy Density Field of Unidirectional Graphite-Epoxy Composite under 9,500 μ -inch Displacement at $x = 2$ -inch.	28
10	Strain Energy Density Field of [0/+15/0] Graphite-Epoxy Composite under 10,500 μ -inch Displacement at $x = 2$ -inch.	29
11	Strain Energy Density Field of [0/+15/0] Graphite-Epoxy Composite under 10,000 μ -inch Displacement at $x = 2$ -inch.	30
12	Strain Energy Density Field of [0/+15/0] Graphite-Epoxy Composite under 9,500 μ -inch Displacement at $x = 2$ -inch.	31

<u>FIGURE</u>		<u>PAGE</u>
13	Strain Energy Density Field of $[0/+30/0]$ Graphite-Epoxy Composite under $10,500 \mu\text{-inch}$ Displacement at $x = 2\text{-inch}$.	32
14	Strain Energy Density Field of $[0/+30/0]$ Graphite-Epoxy Composite under $10,000 \mu\text{-inch}$ Displacement at $x = 2\text{-inch}$.	33
15	Strain Energy Density Field of $[0/+30/0]$ Graphite-Epoxy Composite Under $9,500 \mu\text{-inch}$ Displacement at $x = 2\text{-inch}$.	34
16	Strain Energy Density Field of $[0/+45/0]$ Graphite-Epoxy Composite under $10,500 \mu\text{-inch}$ Displacement at $x = 2\text{-inch}$.	35
17	Strain Energy Density Field of $[0/+45/0]$ Graphite-Epoxy Composite under $10,000 \mu\text{-inch}$ Displacement at $x = 2\text{-inch}$.	36
18	Strain Energy Density Field of $[0/+45/0]$ Graphite-Epoxy Composite under $9,500 \mu\text{-inch}$ Displacement at $x = 2\text{-inch}$.	37
19	Strain Energy Density Field of $[0/+60/0]$ Graphite-Epoxy Composite under $10,500 \mu\text{-inch}$ Displacement at $x = 2\text{-inch}$.	38
20	Strain Energy Density Field of $[0/+60/0]$ Graphite-Epoxy Composite under $10,000 \mu\text{-inch}$ Displacement at $x = 2\text{-inch}$.	39
21	Strain Energy Density Field of $[0/+60/0]$ Graphite-Epoxy Composite under $9,500 \mu\text{-inch}$ Displacement at $x = 2\text{-inch}$.	40
22	Grid Pattern for Analysis of Composite Plate with Hole.	42
23	Stress-Strain Curve for $[0]_8$ Thornel 300/5208 Composite.	46
24	Stress-Strain Curve for $[0/+15/0]_8$ Thornel 300/5208 Composite.	47
25	Stress-Strain Curve for $[0/+30/0]_8$ Thornel 300/5208 Composite.	48
26	Stress-Strain Curve for $[0/+45/0]_8$ Thornel 300/5208 Composite.	49

<u>FIGURE</u>		<u>PAGE</u>
27	Stress-Strain Curve for $[0/\underline{+60}/0]_s$ Thornel 300/5208 Composite.	50
28	Tensile Fatigue Curve for $[0]_g$ Thornel 300/5208 Composite.	52
29	Tensile Fatigue Curve for $[0/\underline{+15}/0]_s$ Thornel 300/5208 Composite.	53
30	Tensile Fatigue Curve for $[0/\underline{+30}/0]_s$ Thornel 300/5208 Composite.	54
31	Tensile Fatigue Curve for $[0/\underline{+45}/0]_s$ Thornel 300/5208 Composite.	55
32	Tensile Fatigue Curve for $[0/\underline{+60}/0]_s$ Thornel 300/5208 Composite	56
33	Static Test Specimens; (a) Static Specimen, (b) A-1-30 (c) b-1-11	58
34	Static Test Specimens; (a) C-1-17, (b) D-1-7 (c) E-1-34	58
35	Static Test Specimens; (a) Fatigue Specimen, (b) A-1-26 (with hole, (c) B-1-2 (with hole)	59
36	Tensile Fatigue Specimens A (25 Hertz); (a) 70% F_{tu} , (b) 62.5% F_{tu} , (c) 55% F_{tu}	60
37	Tensile Fatigue Specimens A (3 Hertz); (a) 70% F_{tu} , (b) 62.5% F_{tu} , (c) 55% F_{tu}	60
38	Tensile Fatigue Specimens B (25 Hertz); (a) 70% F_{tu} , (b) 62.5% F_{tu} , (c) 55% F_{tu}	61
39	Tensile Fatigue Specimens B (3 Hertz); (a) 70% F_{tu} , (b) 62.5% F_{tu} , (c) 55% F_{tu}	61
40	Tensile Fatigue Specimens C (25 Hertz); (a) 70% F_{tu} , (b) 62.5% F_{tu} , (c) 55% F_{tu}	62
41	Tensile Fatigue Specimens C (3 Hertz); (a) 70% F_{tu} , (b) 62.5% F_{tu} , (c) 55% F_{tu}	62
42	Tensile Fatigue Specimens D (25 Hertz); (a) 70% F_{tu} , (b) 62.5% F_{tu} , (c) 55% F_{tu}	63

<u>FIGURE</u>		<u>PAGE</u>
43	Tensile Fatigue Specimens D (3 Hertz); (a) 70% F_{tu} , (b) 62.5% F_{tu} , (c) 55% F_{tu}	63
44	Tensile Fatigue Specimens E (25 Hertz); (a) 70% F_{tu} , (b) 62.5% F_{tu} , (c) 55% F_{tu}	64
45	Tensile Fatigue Specimens E (3 Hertz) ; (a) 70% F_{tu} , (b) 62.5% F_{tu} , (c) 55% F_{tu}	64

SECTION I

INTRODUCTION

The understanding of the failure mechanism of a structural material is basic to design. Static design techniques are assumed to be adequate for structural application; which includes advanced fiber composites. The failure surface concept assumes failure occurs when the load which produces combined stresses falls outside the defined envelope. The stress envelope is produced from simple static test results. The prediction of fatigue failure using a static stress envelope is questionable. Actual failure is established by test of structural components.

The typical structural failure will be induced from stress fields created by discontinuities. Most structural components are subjected to cyclic loading during service. Fatigue cracks, originating from flaws within the composite, are propagated to fracture under cyclic loading conditions. The fatigue or cyclic loading best fits structural design.

Three approaches used in fatigue analysis include: (1) cumulative damage, (2) finite time to crack nucleation, and (3) presence of internal flaws (Fracture Mechanics). Fracture mechanics assumes all materials contain internal flaws with unspecified geometry and distribution. The geometry and distribution of these internal flaws must be established by NDT. Flaws grow in length when the laminate is subjected to load, static or cyclic, until instability occurs. At this point, fast crack propagation occurs and the end result is fracture.

Since the geometry and distribution of internal flaws may not be determined accurately, a flaw of known geometry, is placed in the test specimen to establish failure criteria. Cracks are used as the flaw and the critical stress intensity factor (K_c) determined by experiment. The stress concentration at the tip of the cracks is not defined and makes reproducibility difficult. Slits with known stress concentrations at the tips are used as standards. A simple flaw geometry would be a circular hole in the center of the test specimen. The circular hole allows calculation of the stress concentration distribution and establishes a basis for a generalized failure theory. The stress concentration distribution around the periphery of the hole can be established for static and cyclic loading conditions and varies with composite system, fiber orientation, specimen geometry, diameter of hole, etc. The maximum stress concentration should be the point of crack initiation when considering isotropic materials. The crack will propagate in the field of the smallest strain energy intensity gradient. This would suggest that the crack can propagate in more than one direction (also form more than one crack). Crack instability, however, does not necessarily mean structural failure.

A generalized failure theory should consider as many design variables as possible. These variables would include composite system, fiber orientation (laminate mechanical properties), type of loading, loading conditions (static or cyclic), strain rate or loading frequency, specimen geometry, and flaw size.

Many investigators have outlined failure models for advanced fiber composites considering a specific composite system, a specific loading condition, or extension of metallic (isotropic) failure theories.

An outline of this research is discussed.

1. Theory of Failure

Microscopic fracture analysis has been the subject of a large number of publications since the introduction of the classical theory by Griffith (1). Irwin (2), Cherepanov (3), and Kostrov and Kikitin (4) improved through their analyses, the understanding of the stress state in the vicinity of the crack. Dynamic crack propagation and related phenomena have been reported by such researchers as Goldshtein (5), Cotterell (6), and Daniel (7). The microscopic stress state in a fibrous composite has been studied by Koufopoulos and Theocaris (8), Leissa et al (9), and MacLaughlin (10).

Research, attempting to establish bulk composite strength, has led to the publication of various statistical strength models. Two of these are due to Scop (11) and Friedman (12). Halpin (13) presented an empirical model relating failure loads and time effects statistically.

Macroscopic failure theories have been developed to apply to a given system or application. In general, the theories of failure for isotropic materials have been extended to include anisotropic materials. Most research treats the composite as quasi-homogeneous or as a two-phase system (fiber and matrix). Arbitrary parameters are included in the analyses to produce a failure surface. The Maximum Distortional Energy Theory (Von Mises) is the basis of most analyses. Hill (14) extended the Von Mises theory to include anisotropic materials. Hill produced a failure surface. Azzi and Tsai (15) modified the Hill's criterion to better fit test data. Chamis (16) makes several assumptions and modifies the Von Mises theory to include both tensile and compressive loading condition. Tsai and Wu (17) considers tensile and compressive loading and assumes failure will exist in a stress space.

This produces a modified failure surface. These models are essentially generalizations of the Von Mises criterion adapted to orthotropic plates in plane stress. The models do not specify the mode of failure and does not distinguish between interfacial bond failure, delamination (fracture within the matrix), and simple fiber fracture.

2. Fracture Mechanics Applied to Composites

Fracture mechanics was developed to fill the need within isotropic pressure vessels. Wu (18) found that under specific conditions isotropic fracture mechanics can be applied to anisotropic materials. These conditions include: (1) definite orientation of the flaw with respect to the principal axis, (2) stress intensity factors consistent with isotropic materials, and (3) critical crack orientation coincident with the elastic symmetry. These conditions satisfy the unidirectional fiber orientation only. Unfortunately, conventional isotropic fracture mechanics do not apply in the majority of anisotropic structural applications.

Tetelman (19) outlined the potential fracture mechanisms within fiber composites and related the type of failure to its constituent characteristics. The fiber, matrix, and interfacial behavior under load generate the fracture condition. Zweben (2) presents an analysis of composite tensile strength. Fibers demonstrate strength and length effects leading to at least three modes of composite failure. These modes are: (1) crack propagation in the matrix with few fiber breaks, (2) fiber break propagation, and (3) cumulative damage.

Waddoups, Eisenmann, and Kaminski (21) apply classical fracture mechanics to laminated composites. A circular hole with flaws transverse to the principal axis establishes the point of maximum stress concentration and defines the crack propagation direction. This model insures fulfillment of the specific

conditions required to utilize isotropic fracture mechanics. The model simplifies the analytical approach but is questionable for real application.

Sih et al. (22) investigated the application of fracture mechanics to fiber composite systems using crack models. Existing theory agrees well with glass fiber composite data but graphite fiber composites require a more elaborate model.

Phillips (23) investigated the fracture mechanics of carbon fiber composites. Crack models produced stress intensity factors which agreed well with experimental data. Results differed using natural cracks and "as-cut" cracks.

3. Fatigue

Fatigue failure in metals has been investigated successfully by assuming that a portion of the total strain energy is plastic even at stresses below the proportional limit. Fatigue failure occurs following the application of cyclic loads over a period of time. Saklind (24) reviewed the literature covering fatigue of composites and existing experimental data. Composites are compared to metal fatigue criteria and composites differ in low cycle fatigue. In fact, composites demonstrate a high cycle fatigue strength greater than predicted from metals criteria. Low cycle fatigue is predicted as a critical design factor for composites.

Holmes and Wright (25) tested several angle-ply graphite-epoxy specimens in fatigue and concluded that the observed secondary failure. Primary failure was by tension at the reduced cross-section.

Several strength criteria have been postulated for composites. In most cases these criteria are assumed to be valid for static as well as dynamic loading. Many investigators have modified the Von Mises yield criterion for

orthotropic materials. Sendeckyj (26) has reviewed these and other strength criteria for composites.

Hashin and Rotem (27) present a simple failure criterion involving a fiber failure mode and a matrix failure mode. The failure criterion agrees well with glass fiber composite fatigue data.

SECTION II

TECHNICAL APPROACH

The investigation of the fatigue strength of multilayer advanced fiber composites should consider all possible variables. These variables include composite system, fiber orientation, specimen geometry, hole size, type of loading, fatigue loading conditions and loading frequency. To observe the effect of individual variables, as many of the remaining parameters must be held constant as possible. In this manner, the primary parameters are defined and incorporated into a generalized failure theory.

The composite system considered was the graphite-epoxy (Thornel 300/5208) system. Other systems should be investigated to establish primary failure modes.

Two test specimen configurations were used in the research. The static specimen was 6.5-inch x 1-inch and eight (8) plies in thickness. These specimens contained no circular holes. The fatigue specimen was of similar geometry containing a 3/16-inch diameter hole in the center position. Aluminum grips were bonded on the ends of the specimens. These specimens are shown in Figure 1.

All specimens contained a general fiber orientation of $[0/\pm\theta/0]_s$. The angle θ is measured between the longitudinal axis and the oriented fibers. The fiber orientations considered were:

$[0]_g$ unidirectional

$[0/\pm 15/0]_s$

$[0/\pm 30/0]_s$

$[0/\pm 45/0]_s$

$[0/\pm 60/0]_s$

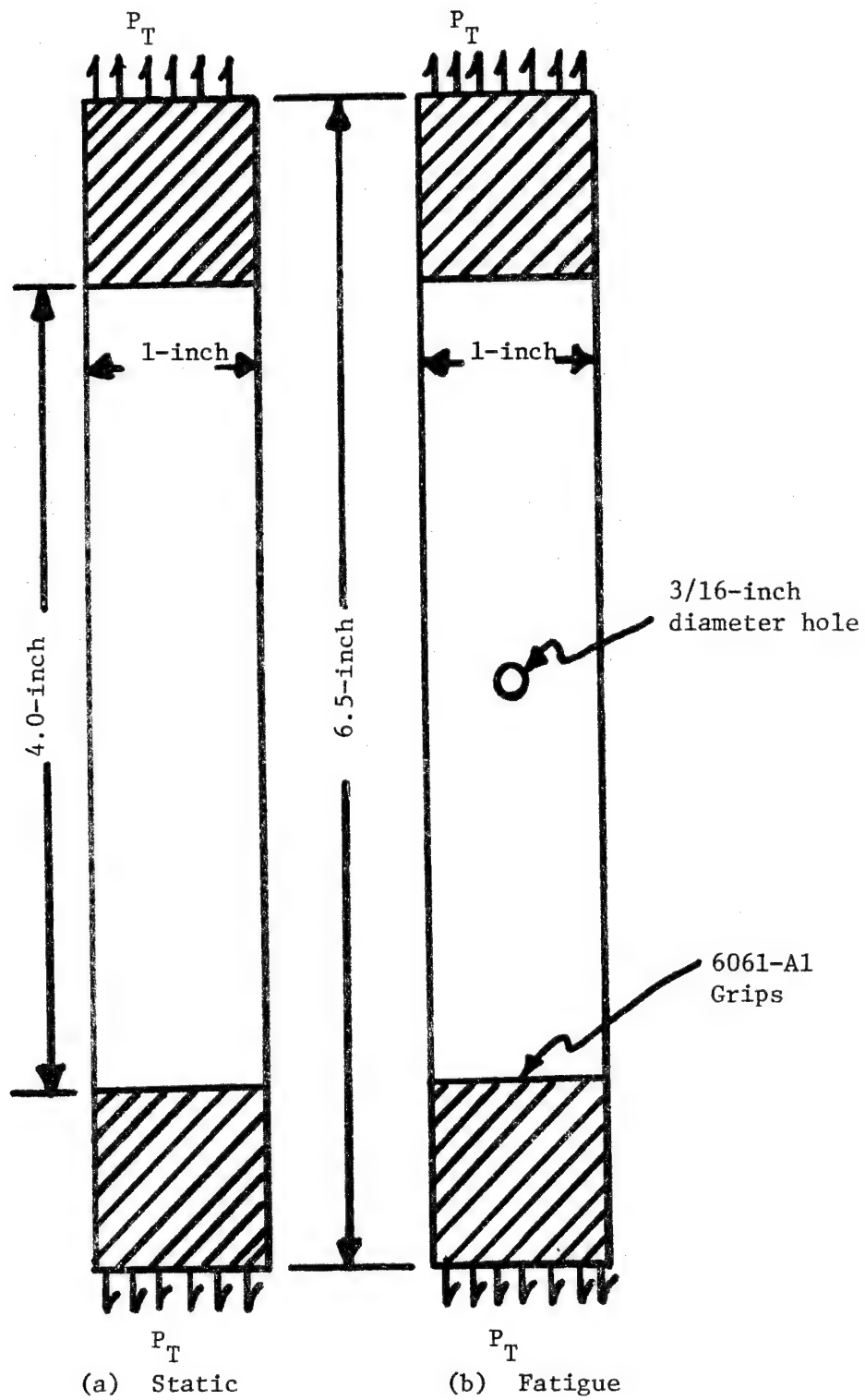


Figure 1. Composite Test Specimen Configuration

The specimen configuration and the hole size are fixed with varying fiber orientations.

The static test specimens (no hole) are required to establish the elastic constants necessary for analysis. The fatigue specimens (with hole) are used to investigate the fatigue strength and failure modes. A sinusoidal loading function of basically tension-zero-tension was applied axially to the specimens. A small tensile load was applied at the minimum stress to insure against compressive loads. The maximum stresses used were 70%, 62.5%, and 55% of the ultimate tensile stress of the static specimen. Two loading frequencies, 3 and 25 Hertz, were investigated to examine low-frequency and high-frequency tensile fatigue effects.

The static and fatigue test specimens were modeled and analyzed. Analytical characterization of the following anisotropic plates were considered. Included were:

- static - no hole
- dynamic - no hole

- static - hole infinite plate
- dynamic - hole infinite plate

- static - hole finite plate
- dynamic - hole finite plate

These analytical models consider all possibilities of tensile loading for the static and fatigue test specimens.

SECTION III

ANALYTICAL CHARACTERIZATION

The analytical characterization of the load and deformation distributions within a multilayer fiber composite plate was examined for static and dynamic loading conditions. The generalized anisotropic plate analysis for static loading conditions without a flaw (circular hole) was developed to define the field equations and boundary conditions necessary for further analytical development. The analysis considers the linearly exact relations resulting in the equilibrium equations. The constitutive equations are outlined for a laminated medium. The field equations and boundary conditions are based on the Kirchhoff hypothesis. The constitutive equation coefficients are defined for the composite system $[0/\pm\theta/0]_s$. This composite system is basic to this research. These equations are basic for the static loading condition.

The field equations and boundary conditions were derived for a dynamically loaded anisotropic plate with and without a circular hole. The hole in an infinite plate or a hole in a finite plate becomes a matter of definition and application of the appropriate boundary conditions. All systems, whether static or dynamic loading or with or without circular hole, should relate to the generalized anisotropic plate analysis when the proper boundary conditions are used.

The generalized anisotropic plate analysis defines the field equations and boundary conditions for the static loaded anisotropic plate (no hole). The homogeneous set of equations was analyzed using the finite difference method. The dynamic stress field in the composite considered one-dimensional loading.

A finite difference method was used in an effort to solve the field equations for the static and dynamic models containing a circular hole. The boundary conditions around the periphery of the hole were difficult to specify.

1. Nomenclature

b_{11}^* , b_{12}^* , b_{22}^* - elastic constants

C_{11} , C_{12} , C_{66} - elastic constants

h - thickness

k_1 , k_2 , k_3 - constant

L - length

M - stress moment

N - applied moment

P - applied tractions

R - radius of hole

t - time

T - stress resultant

u, v - displacements in x and y direction

x, y, z - coordinates

α, β - constants

ϵ_{xx} , ϵ_{yy} - in-plane strains

ω - frequency

ρ - mass density

σ - applied stress

θ, ϕ - angles

ν - Poisson's ratio

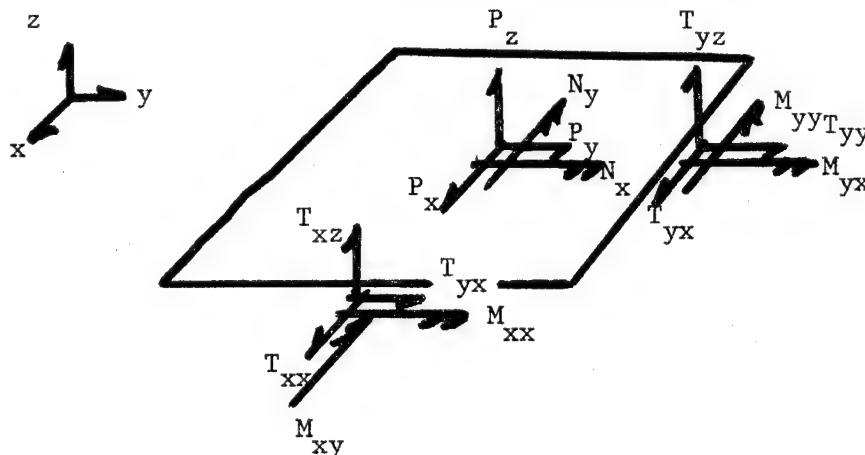
2. Generalized Anisotropic Plate Analysis

2.1 Elastic Constants

The generalized anisotropic plate analysis is generated for a plate of thickness "h" and the reference surface is at the mid plane. The linearly exact relations are defined in terms of stress resultants [28]. The stress resultants are defined in terms of stresses. The equilibrium and compatibility relations are defined at the reference surface. Hooke's law is written for an orthotropic material. The rotational transformation law for elastic constants has been reported by Tsai [29].

The constitutive equations are considered for a layered medium. The field equations and boundary conditions for off angle layers symmetrically layed-up are identified from the analysis. The field equations can be derived for the static as well as the dynamic case.

The equations for the determination of the elastic constants by axial test can now be considered. For purposes of determining the elastic constants, b_{11}^* , b_{12}^* , b_{22}^* , two types of tensile specimens are required. The first will have all fibers longitudinal to the load (0°) and the other will have the fibers transverse to the load (90°). A sketch of the coupon with dimensions and coordinate axis is shown as follows.



The strain expressions which satisfy the field equations and boundary conditions are given as follows.

$$\epsilon_{xx} = \frac{C_{22}}{(C_{11}C_{22} - C_{12}^2)} \frac{p}{b} \quad (2-1)$$

$$\epsilon_{yy} = \frac{-C_{12}}{(C_{11}C_{22} - C_{12}^2)} \frac{p}{b}$$

For the 0° direction

$$\epsilon_{xx}^{\circ} = \frac{b_{22}^*}{(b_{11}^* b_{22}^* - b_{12}^{*2})} \frac{p^{\circ}}{8bh} \quad (2-2)$$

$$\epsilon_{yy}^{\circ} = \frac{-b_{12}^*}{(b_{11}^* b_{22}^* - b_{12}^{*2})} \frac{p^{\circ}}{8bh}$$

For the 90° direction

$$\epsilon_{xx}^{90} = \frac{b_{11}^*}{(b_{11}^* b_{22}^* - b_{12}^{*2})} \frac{p^{90}}{8bh} \quad (2-3)$$

$$\epsilon_{yy}^{90} = \frac{-b_{12}^*}{(b_{11}^* b_{22}^* - b_{12}^{*2})} \frac{p^{90}}{8bh}$$

Solving for elastic constants, the result becomes the following.

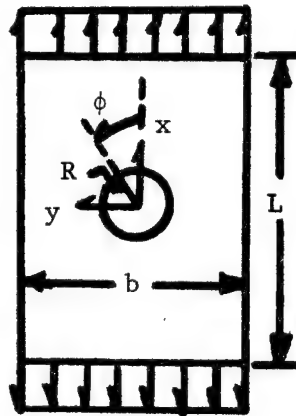
$$b_{11}^* = \frac{\frac{\epsilon_{xx}^{90}}{p^{90}}}{8bh \left[\left(\frac{\epsilon_{xx}^{\circ}}{p^{\circ}} \right) \left(\frac{\epsilon_{xx}^{90}}{p^{90}} \right) - \frac{1}{4} \left(\frac{\epsilon_{yy}^{\circ}}{p^{\circ}} + \frac{\epsilon_{yy}^{90}}{p^{90}} \right)^2 \right]}$$

$$b_{22}^* = \frac{\frac{\epsilon_{xx}^{\circ}}{p^{\circ}}}{8bh \left[\left(\frac{\epsilon_{xx}^{\circ}}{p^{\circ}} \right) \left(\frac{\epsilon_{xx}^{90}}{p^{90}} \right) - \frac{1}{4} \left(\frac{\epsilon_{yy}^{\circ}}{p^{\circ}} + \frac{\epsilon_{yy}^{90}}{p^{90}} \right)^2 \right]} \quad (2-4)$$

$$b_{12}^* = \frac{-\frac{1}{2} \left(\frac{\epsilon_{yy}^0}{p^0} + \frac{\epsilon_{yy}^{90}}{p^{90}} \right)}{8bh \left[\left(\frac{\epsilon_{xx}^0}{p^0} \right) \left(\frac{\epsilon_{xx}^{90}}{p^{90}} \right) - \frac{1}{4} \left(\frac{\epsilon_{yy}^0}{p^0} + \frac{\epsilon_{yy}^{90}}{p^{90}} \right)^2 \right]}$$

2.2 Governing Equations for a Laminate with Hole and Symmetrically Loaded

The field equations and boundary conditions are outlined for a dynamically loaded 8-ply symmetrically layed-up composite plate. The lay-up for the half thickness is $[0/\pm\theta/0]$. A circular hole of radius "R" is assumed to exist in the plate and a uniaxial membrane excitation is imposed on one end of the plate. Thermal effects, bending, body forces and surface tractions are neglected. A diagram of the plate is shown as follows.



$$\sigma = \sigma(t)$$

The field equations, assuming "equivalent homogeneity" through the thickness, become:

$$\begin{aligned} C_{11} \frac{\partial^2 u}{\partial x^2} + C_{66} \frac{\partial^2 u}{\partial y^2} + (C_{12} + C_{66}) \frac{\partial^2 v}{\partial x \partial y} &= 8\rho h \frac{\partial^2 u}{\partial t^2} \\ (C_{12} + C_{66}) \frac{\partial^2 u}{\partial x \partial y} + C_{66} \frac{\partial^2 v}{\partial x^2} + C_{22} \frac{\partial^2 v}{\partial y^2} &= 8\rho h \frac{\partial^2 v}{\partial t^2} \end{aligned} \quad (2-5)$$

The boundary conditions are:

(1) Stress conditions at edges

$$\begin{aligned}
 T_{yy}(x, \pm \frac{b}{2}, t) &= 0 & T_{rr}(R, \phi, t) &= 0 \\
 T_{xy}(x, \pm \frac{b}{2}, t) &= 0 & T_{r\theta}(R, \phi, t) &= 0 \\
 T_{xy}(\pm \frac{L}{2}, y, t) &= 0 \\
 T_{xx}(\pm \frac{L}{2}, y, t) &= 8h\sigma(t)
 \end{aligned} \tag{2-6}$$

(2) The stress boundary conditions in terms of displacements are:

$$\begin{aligned}
 [C_{12} \frac{\partial u}{\partial x} + C_{22} \frac{\partial v}{\partial y}]_{(x, \pm \frac{b}{2}, t)} &= 0 \\
 [\frac{\partial u}{\partial y} + \frac{\partial v}{\partial x}]_{(x, \pm \frac{b}{2}, t)} &= 0 \\
 [\frac{\partial u}{\partial x} + \frac{\partial v}{\partial x}]_{(\pm \frac{L}{2}, y, t)} &= 0 \\
 [C_{11} \frac{u}{x} + C_{12} \frac{v}{y}]_{(\pm \frac{L}{2}, y, t)} &= 8h\sigma(t) \\
 [(C_{11} \cos^2 \phi + C_{12} \sin^2 \phi) \frac{u}{x} + (2C_{66} \cos \phi \sin \phi) \frac{\partial u}{\partial y} + \\
 (C_{22} \sin^2 \phi + C_{12} \cos^2 \phi) \frac{\partial v}{\partial y} + (2C_{66} \cos \phi \sin \phi) \frac{\partial v}{\partial x}]_{(R, \phi, t)} &= 0 \\
 [C_{66} (\cos^2 \phi \sin^2 \phi) \frac{\partial u}{\partial y} - (C_{11} - C_{12}) \cos \phi \sin \phi \frac{\partial u}{\partial x} + \\
 C_{66} (\cos^2 \phi - \sin^2 \phi) \frac{\partial v}{\partial x} + (C_{22} - C_{12}) \cos \phi \sin \phi \frac{\partial v}{\partial y}]_{(R, \phi, t)} &= 0
 \end{aligned} \tag{2-7}$$

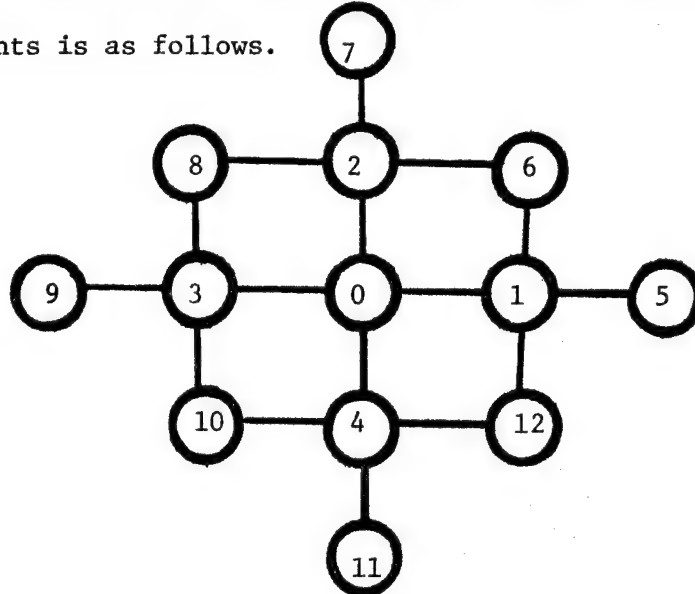
The boundary conditions consider a free outside boundary and the expressions are the same with or without a circular hole.

3. Dynamic Plate Model - No Hole

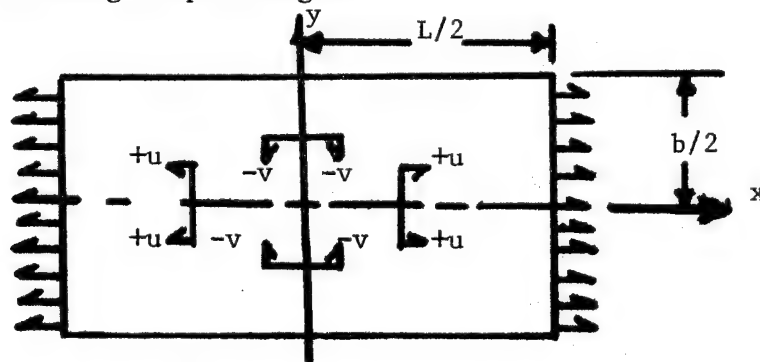
The homogeneous set of equation (2-5) was expressed in finite difference form and was solved by iteration. The finite difference form of equation (2-5) is as follows:

$$\begin{aligned}
 & c_{11} \left(\frac{u_3 - 2u_0 + u_1}{\Delta x^2} \right) + c_{66} \left(\frac{u_2 - 2u_0 + u_4}{\Delta y^2} \right) \\
 & + (c_{12} + c_{66}) \left(\frac{v_6 + v_{10} - v_{12} - v_8}{4\Delta x \Delta y} \right) = 0 \\
 & (c_{12} + c_{66}) \left(\frac{u_6 + u_{10} - u_{12} - u_7}{4\Delta x \Delta y} \right) + c_{66} \left(\frac{v_3 - 2v_0 + v_1}{\Delta x^2} \right) \\
 & + c_{22} \left(\frac{v_2 - 2v_0 + v_4}{\Delta y^2} \right) = 0
 \end{aligned} \tag{3-1}$$

where the general fourth order finite difference representation molecule used for internal points is as follows.



Calculation of displacements was considered for the upper-right (+,+) quadrant of the following coupon diagram.



The boundary conditions used were:

- (1) u displacements are symmetric across x axis and antisymmetric across y axis.
- (2) v displacements are symmetric across y axis and antisymmetric across x axis.
- (3) u displacements on the y centerline are zero; v displacements on the x centerline and at $x = L/2$ are zero.
- (4) applied displacement at $x = L/2$ is $u = u_0 + k \sin(\omega t + \phi_1)$ where u_0 is initial displacement, $u_0 = 0.01000$ inches, k_1 is a suitable constant (0.00050 inches), ω is the circular forcing frequency, t is time, and ϕ_1 is a phase angle (0 radians).
- (5) the free boundary of the quadrant was taken as

$$v = [k_2 + k_3 \sin(\omega t + \phi_2)] e^{\alpha x - \beta t} \quad (3-2)$$

where k_2, k_3, α, β are constants and ϕ_2 is a phase angle (0 radians).

This boundary condition was calculated to match the magnitude of displacements observed at the y centerline of the static tensile tests. Displacement u on the free boundary was determined using equation 2-7. The equation is:

$$\left[\frac{\partial u}{\partial x} + \frac{\partial v}{\partial x} \right]_{\left(\frac{L}{2}, \frac{b}{2}, t \right)} = 0$$

The displacements were assumed to vary as $\left(\frac{x}{L/2} \right)^{1/2}$ from a value of zero at $x = 0$ to a maximum given by the boundary conditions evaluated at $x = L/2$. For u displacements, the following equation was used.

$$u = \frac{b}{\alpha^2} (k_2 + k_3 \sin(\omega t + \phi_2)) (e^{\alpha x - \beta t} - e^{\frac{\alpha L}{2} - \beta t}) + u_0 + k_1 \sin \omega t + \phi \left(\frac{2x}{L} \right)^{1/2} \quad (3-3)$$

Values of the constants used were:

$$\alpha = -1.5000$$

$$\beta = 6.000$$

$$k_2 = 1.000$$

$$k_3 = 0.5000$$

(6) the v displacements along the y centerline were taken as a linear function of " y " and the u displacements were assumed to be linear functions of " x " along the x centerline. Along the x centerline, the u displacements were

$$u = \frac{2x}{L} [u_0 + k_1 \sin(\omega t + \phi_1)]$$

Along the y centerline, v displacements were:

$$v = -\frac{2y}{b} [k_2 + k_3 \sin(\omega t + \phi_2)] e^{-\beta}$$

The homogeneous set of field equations corresponding to the static case was solved by advancing time to achieve required boundary displacements and then iterating for the displacement field. Calculations were made at the nodes of a 4×4 grid in the upper right quadrant (25 points). Convergence giving three significant figures occurred in 20 iterations. Approximately 10 seconds of computer time was required per static field.

In order to solve the nonhomogeneous set of field equations (2-5) corresponding to time dependency, the inertia terms of the right hand side of the equations were taken as:

$$\begin{aligned} 8\rho h \frac{\partial^2 u}{\partial t^2} &= f_1(t) f_1(x,y) \\ 8\rho h \frac{\partial^2 v}{\partial t^2} &= f_2(t) f_2(x,y) \end{aligned} \quad (3-4)$$

By solving the first of the field equations for $\frac{\partial^2 v}{\partial x^2}$ and $\frac{\partial^2 v}{\partial y^2}$ and substituting into the second equation, the following results.

$$\frac{\partial^4 u}{\partial x^4} - \frac{[C_{66}^2 + (C_{12} + C_{66})^2 - C_{11}C_{22}]}{C_{11}C_{66}} \frac{\partial^4 u}{\partial x^2 \partial y^2} + \frac{C_{22} \partial^4 u}{C_{11} \partial y^4} -$$

$$\begin{aligned} & \left(\frac{C_{12} + C_{66}}{C_{11} C_{66}} \right) \left[\left(\frac{C_{66}}{C_{12} + C_{66}} \right) \frac{\partial^2}{\partial x^2} (F_1(t) F_1(x,y)) + \right. \\ & \left. \left(\frac{C_{22}}{C_{12} + C_{66}} \right) \frac{\partial^2}{\partial y^2} (F_1(t) F_1(x,y)) - \frac{\partial^2 (F_2(t) F_2(x,y))}{\partial x \partial y} \right] = 0 \end{aligned} \quad (3-5)$$

By solving the second equation for $\frac{\partial^2 u}{\partial x^2}$ and $\frac{\partial^2 u}{\partial y^2}$ and substituting into the first, the following results.

$$\frac{\partial^4 v}{\partial x^4} - \left[\frac{C_{66}^2 + (C_{12} + C_{66})^2 - C_{11} C_{22}}{C_{11} C_{66}} \right] \frac{\partial^4 v}{\partial x^2 \partial y^2} + \quad (3-6)$$

$$\frac{C_{22}}{C_{11}} \frac{\partial^4 v}{\partial y^4} - \left(\frac{C_{12} + C_{66}}{C_{11} C_{66}} \right) \left[\left(\frac{C_{11}}{C_{12} + C_{66}} \right) \frac{\partial^2}{\partial x^2} (F_2(t) F_2(x,y)) + \right.$$

$$\left. \left(\frac{C_{66}}{C_{12} + C_{66}} \right) \frac{\partial^2}{\partial y^2} (F_2(t) F_2(x,y)) - \frac{\partial^2}{\partial x \partial y} F_1(t) F_1(x,y) \right] = 0$$

The following substitutions were made into equations 3-5 and 3-6.

$$\begin{aligned} F_1(t) F_1(x,y) &= k_5 \rho h \omega_n^2 \cos(\omega_n t) \sin\left(\frac{\pi}{L} x\right) \cos\left(\frac{\pi L}{b} y - \frac{2\pi y}{b} x\right) \\ F_2(t) F_2(x,y) &= k_5 \rho h \omega_n^2 \cos(\omega_n t) \sin\left(\frac{\pi y}{b}\right) \cos\left(\frac{\pi}{L} x\right) \end{aligned} \quad (3-7)$$

The natural frequency of the coupon is ω_n and k_5 is equal to 80.00.

Orthotropic plate velocity was used by Reuter [30] to determine displacement fields.

Time dependent boundary conditions of the forcing function were applied.

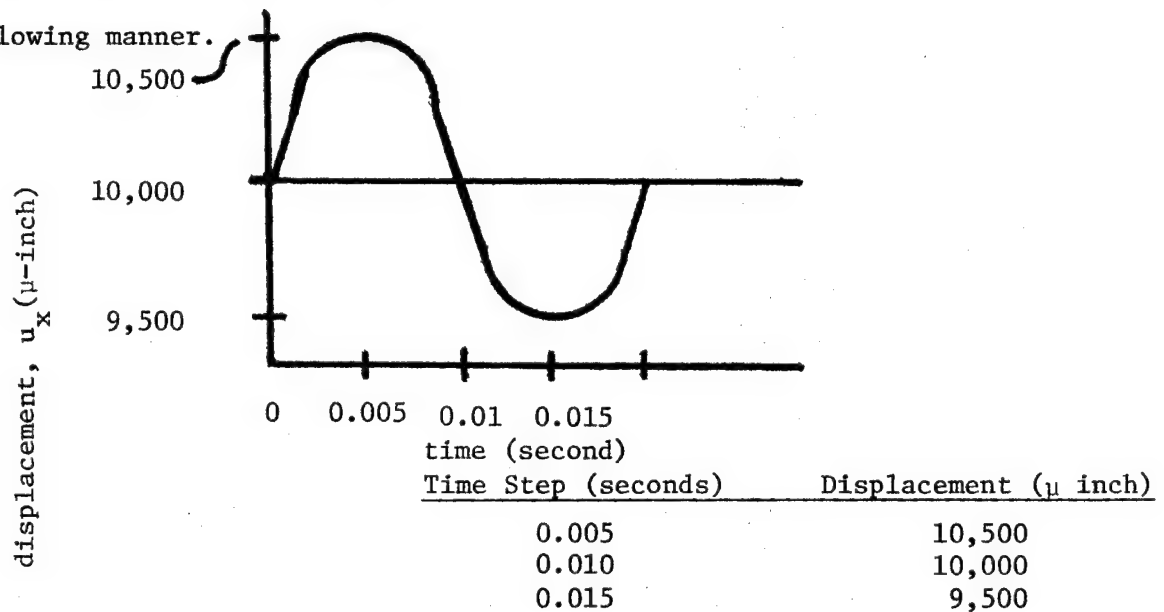
A time increment is $\Delta x = \frac{\pi}{2\omega} = \frac{\text{load cycle}}{4}$. Addition of the inertia

terms required further iteration to establish displacements in the quadrant.

Strain energy densities were calculated for the one quadrant.

The strain energy density fields for the static loading ($t=0$) of the $[0/+0/0]_S$ graphite-epoxy composite systems are shown in Figures 2-6. The graphite-epoxy specimens deform approximately 10,000 μ -inch (at $x = 2$ inch) prior to fracture. The σ_x , σ_y , and σ_{xy} stress fields were also determined but not included in this report.

The dynamic strain energy density fields for the graphite-epoxy composite systems were determined for a loading frequency of 50 Hertz, considering time steps of 0.005, 0.010, and 0.015 seconds. The static displacement ($t=0$) of 10,000 μ -inch at $x = 2$ -inch was deformed in the following manner.



The strain energy density fields for the three (3) time steps are shown in Figures 7-21. The change in the strain energy density contours with time notes the microscopic variance which relates to fatigue characteristics.

A failure criterion was proposed correlating the strain energy release rate (G) and the strain energy density. It is assumed that the strain energy release rate is proportional to the strain energy density.

$$\left(\frac{\text{in-lb}}{\text{in}^3}\right) \times 10^3$$

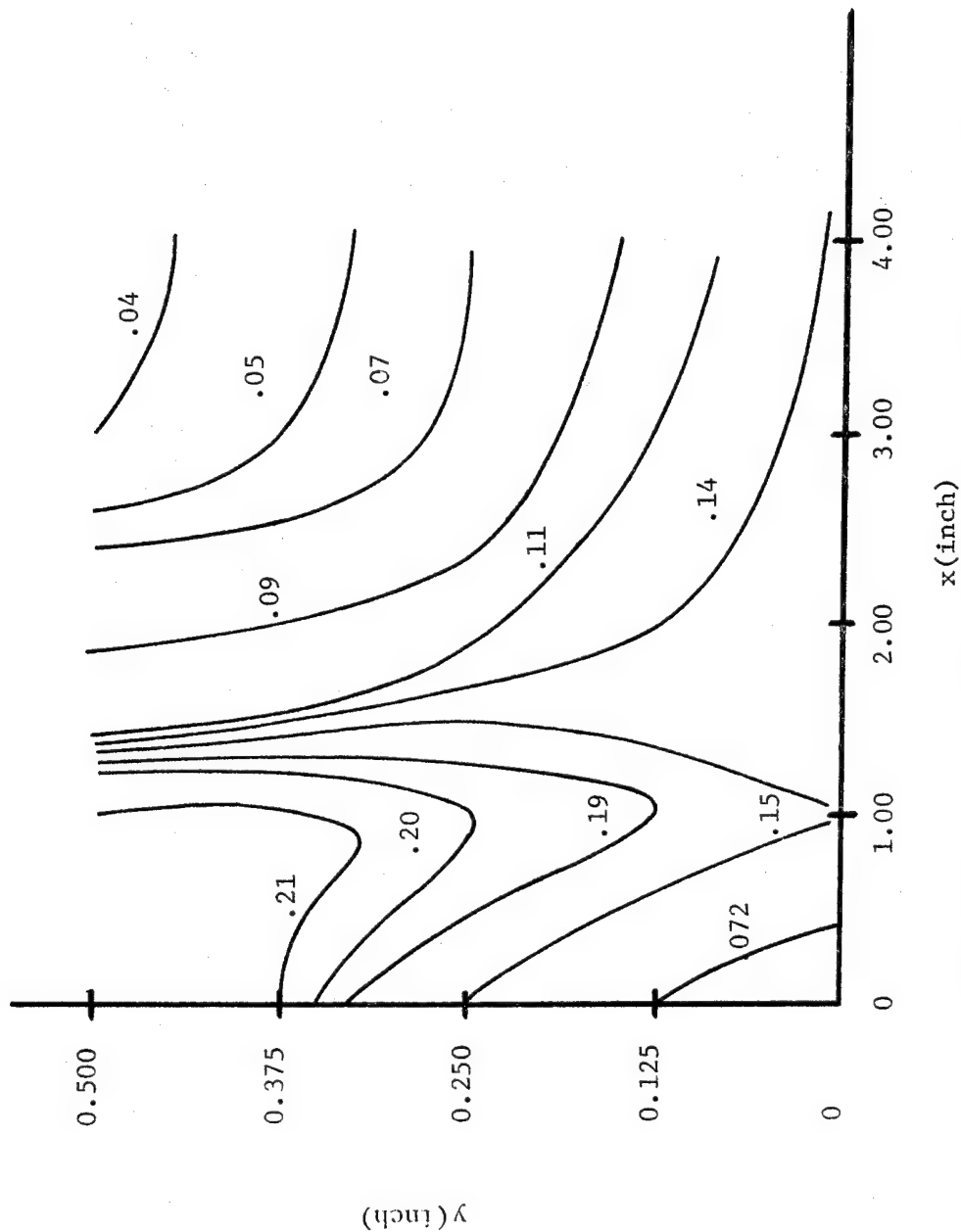


Figure 2. Strain Energy Density Field of Unidirectional Graphite-Epoxy Composite under 10,000 μ -inch Displacement at $x = 2$ -inch.

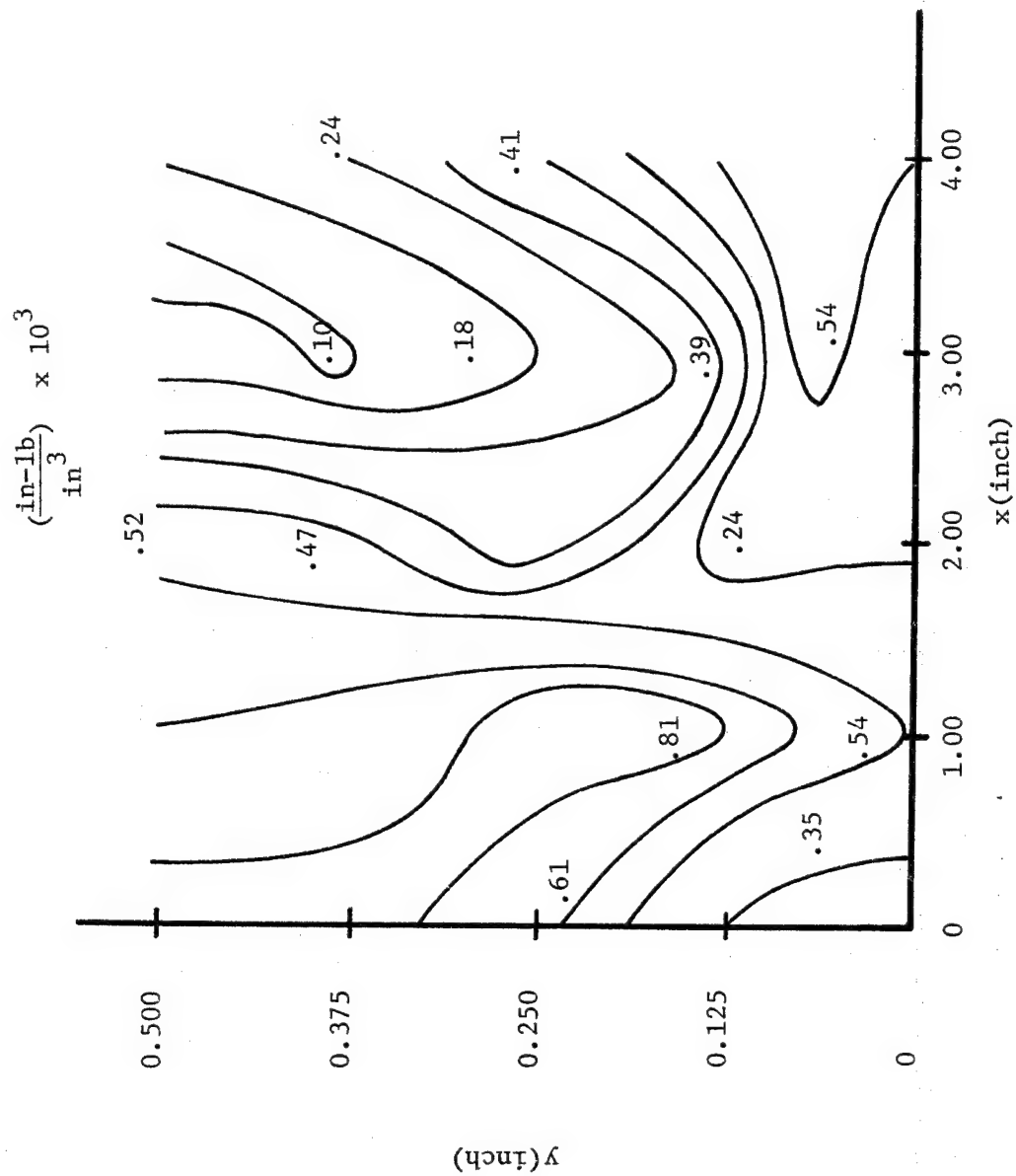


Figure 3. Strain Energy Density Field of $[0/+15/0]$ Graphite-Epoxy Composite under 10,000 $\mu\text{-inch}$ Displacement at $x = 2\text{-inch}$.

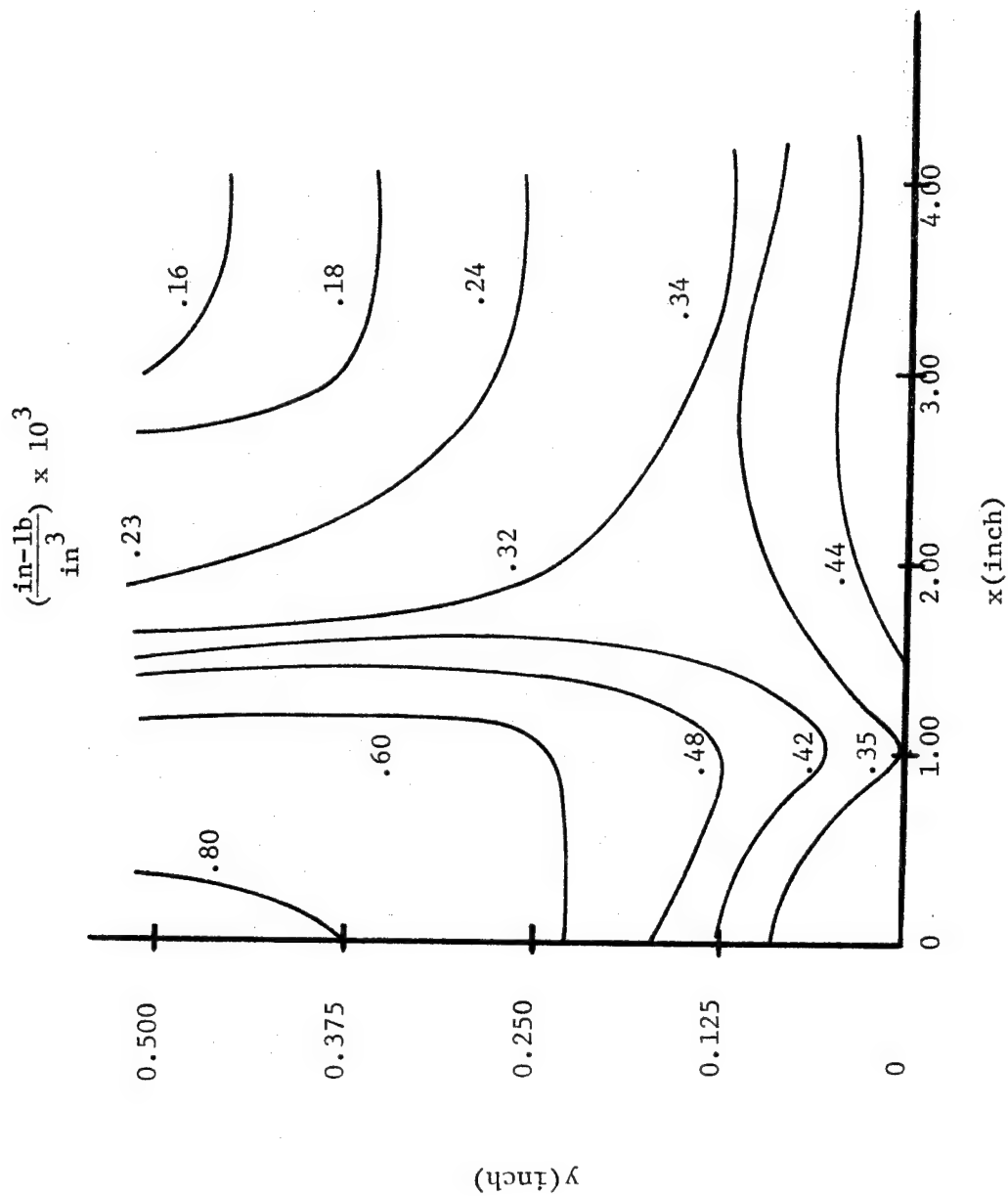


Figure 4. Strain Energy Density Field of $[0/+30/0]_S$ Graphite-Epoxy Composite under 10,000 μ -inch Displacement at $x = 2$ -inch.

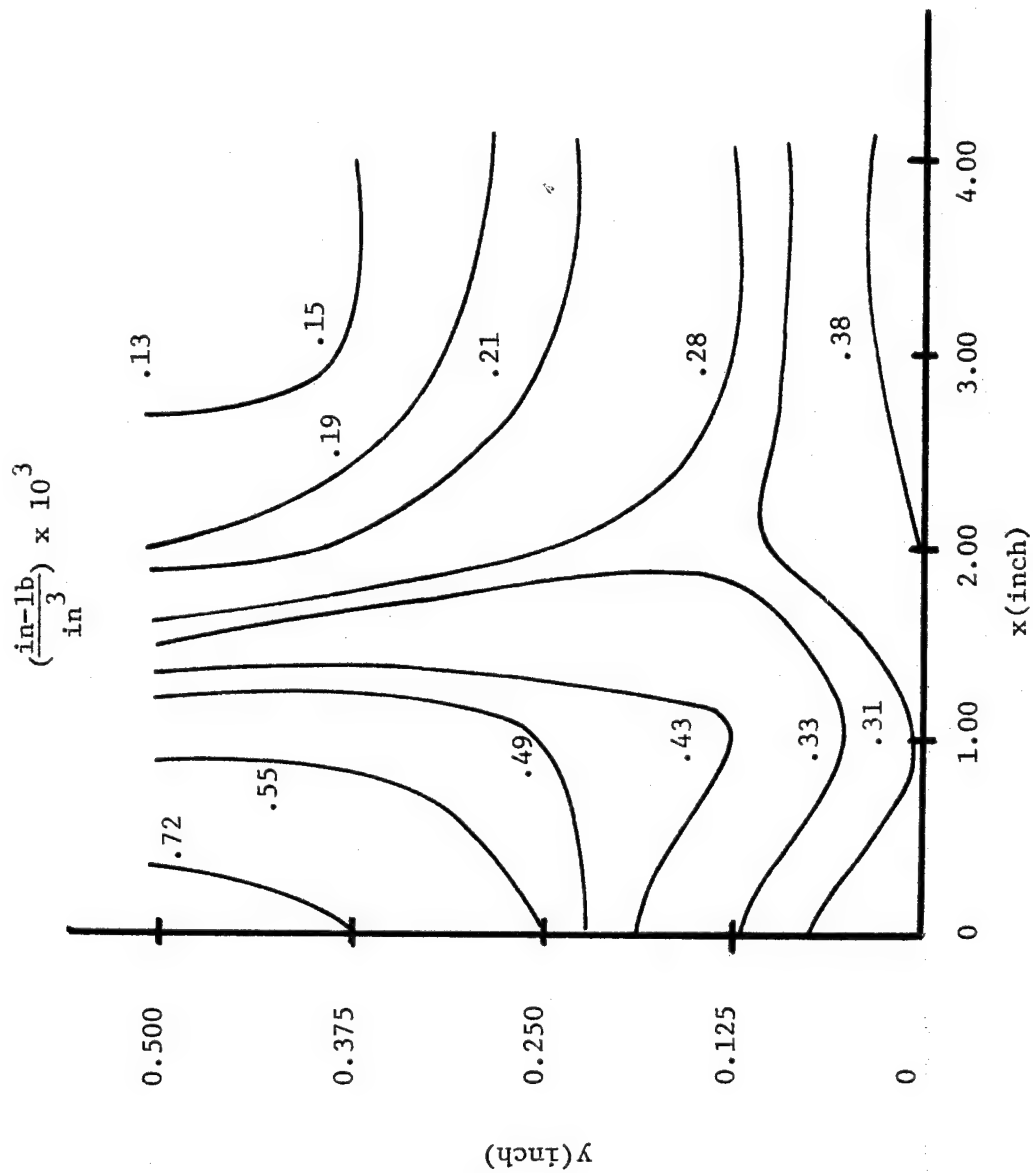


Figure 5. Strain Energy Density Field of $[0/+45/0]_s$ Graphite-Epoxy Composite under 10,000 $\mu\text{-inch}$ Displacement at $x = 2$ inch

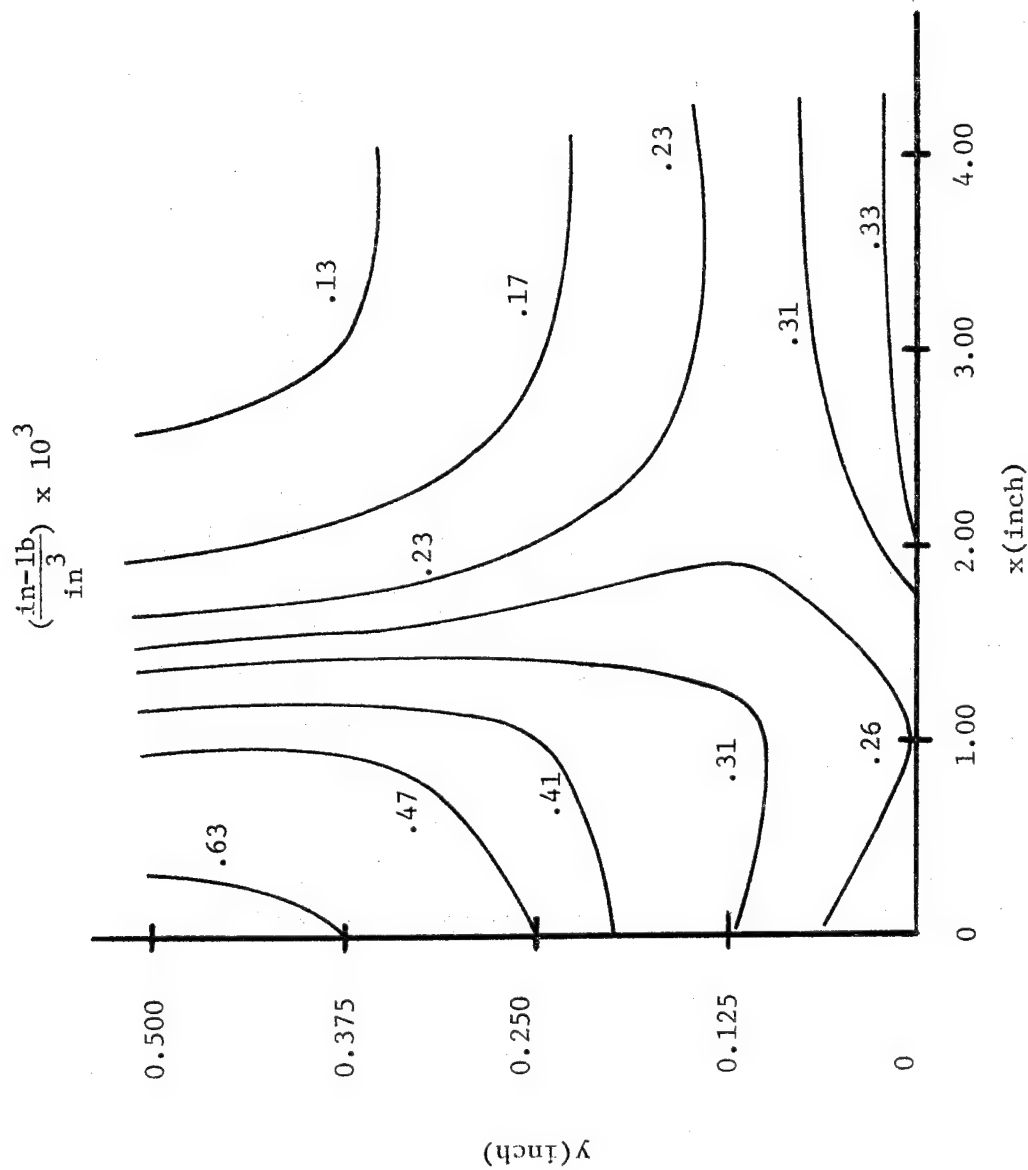


Figure 6. Strain Energy Density Field of [0/+60/0] Graphite-Epoxy Composite under 10,000 μ -inch Displacement at $x = 2$ -inch.

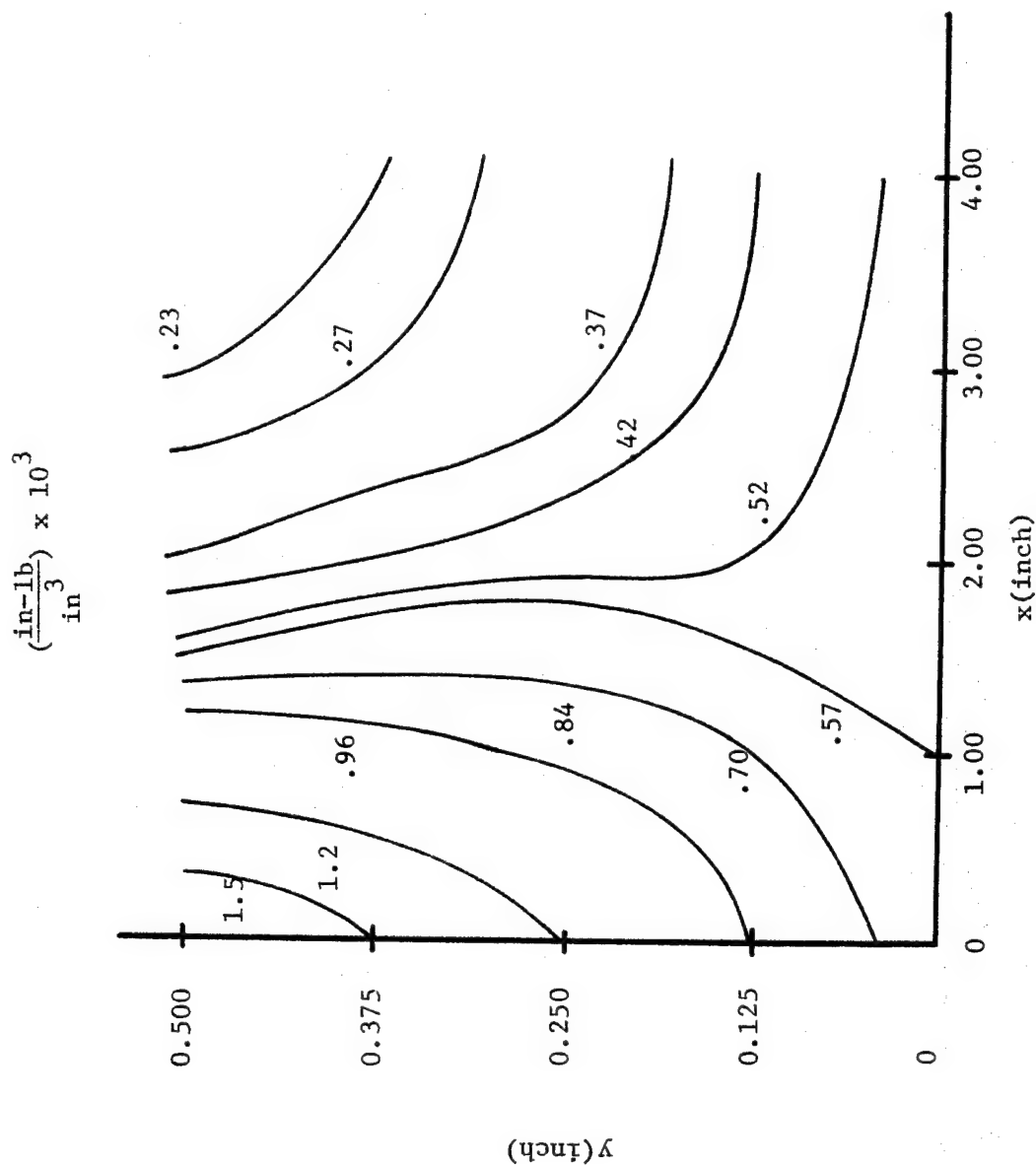


Figure 7. Strain Energy Density Field of Unidirectional Graphite-Epoxy Composite under 10,500 μ -inch Displacement at = 2 inch.

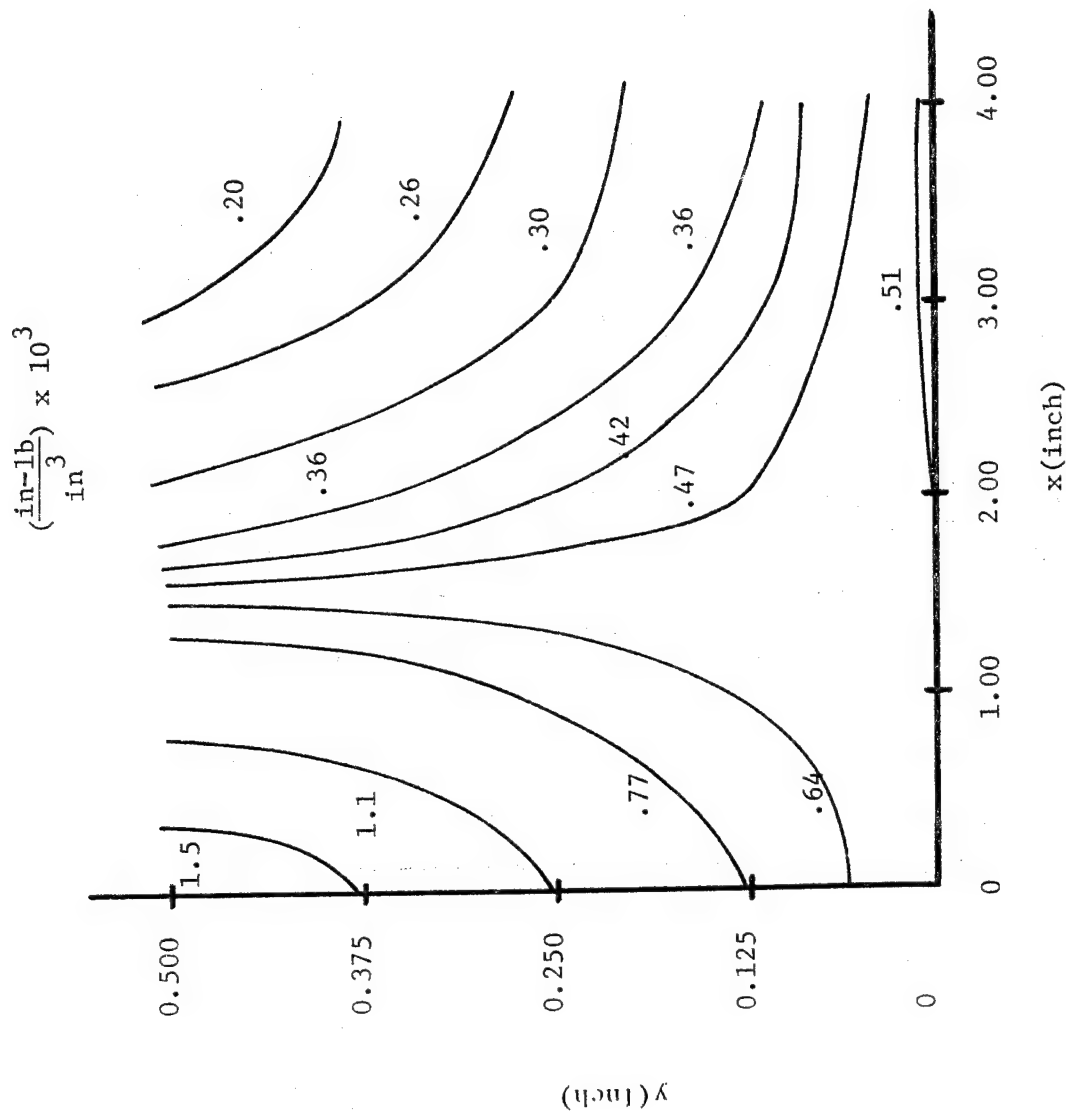


Figure 8. Strain Energy Density Field of Unidirectional Graphite-Epoxy Composite under 10,000 μ -inch Displacement at $x = 2$ -inch

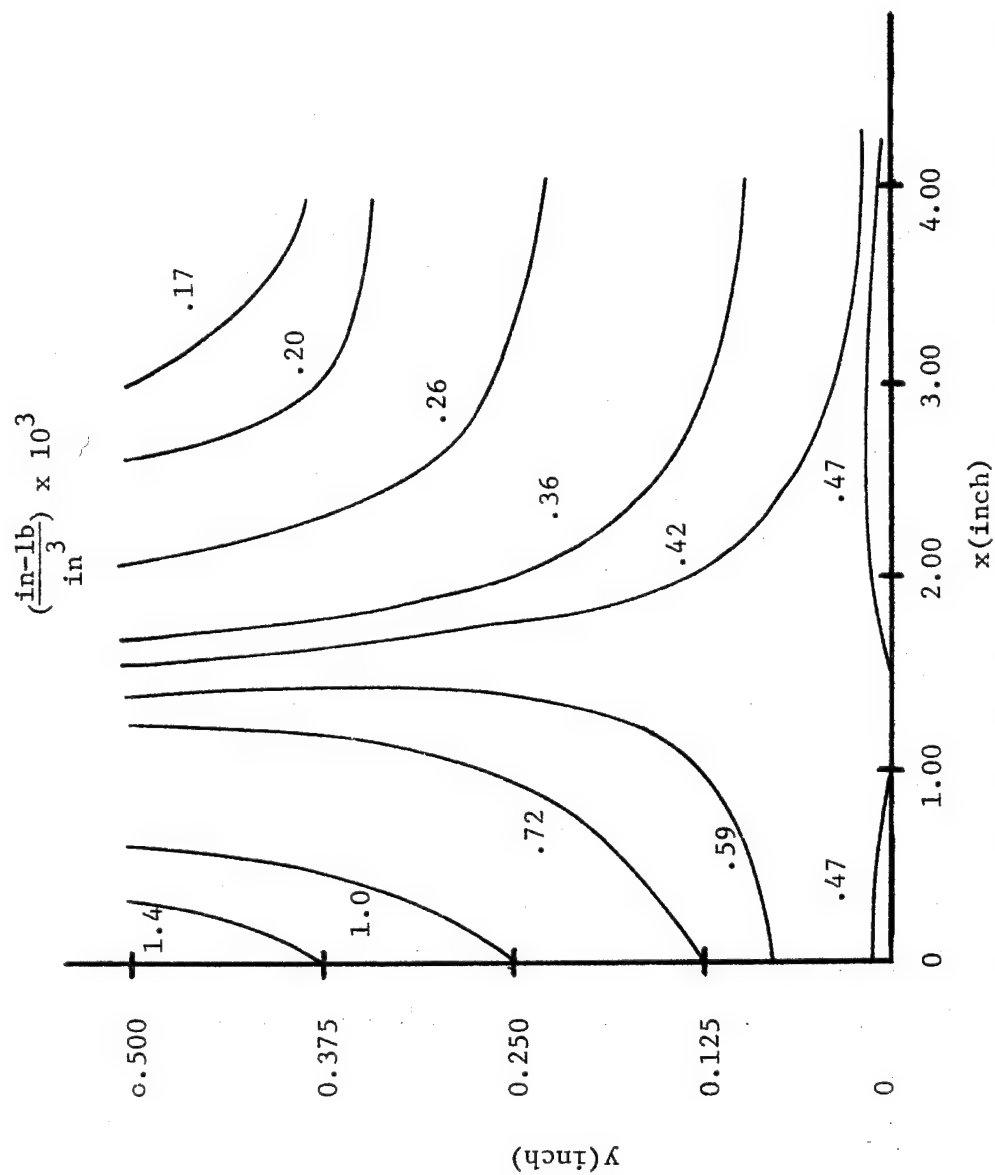


Figure 9. Strain Energy Density Field of Unidirectional Graphite-Epoxy Composite under 9,500 μ -inch Displacement at $x = 2$ -inch

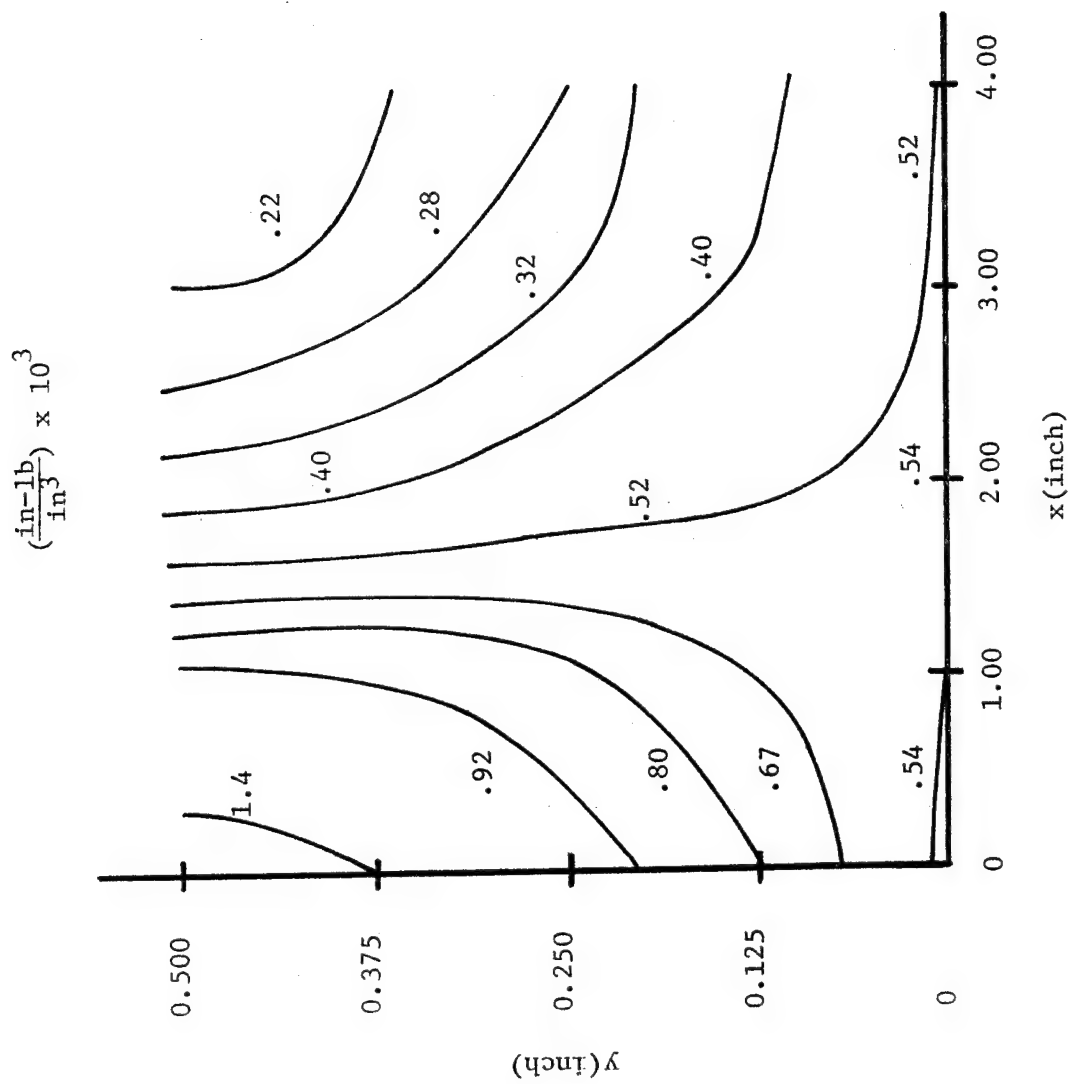


Figure 10. Strain Energy Density Field of $[0/+15/0]_s$ Graphite-Epoxy Composite under 10,500 μ -inch Displacement at $x = 2$ -inch.

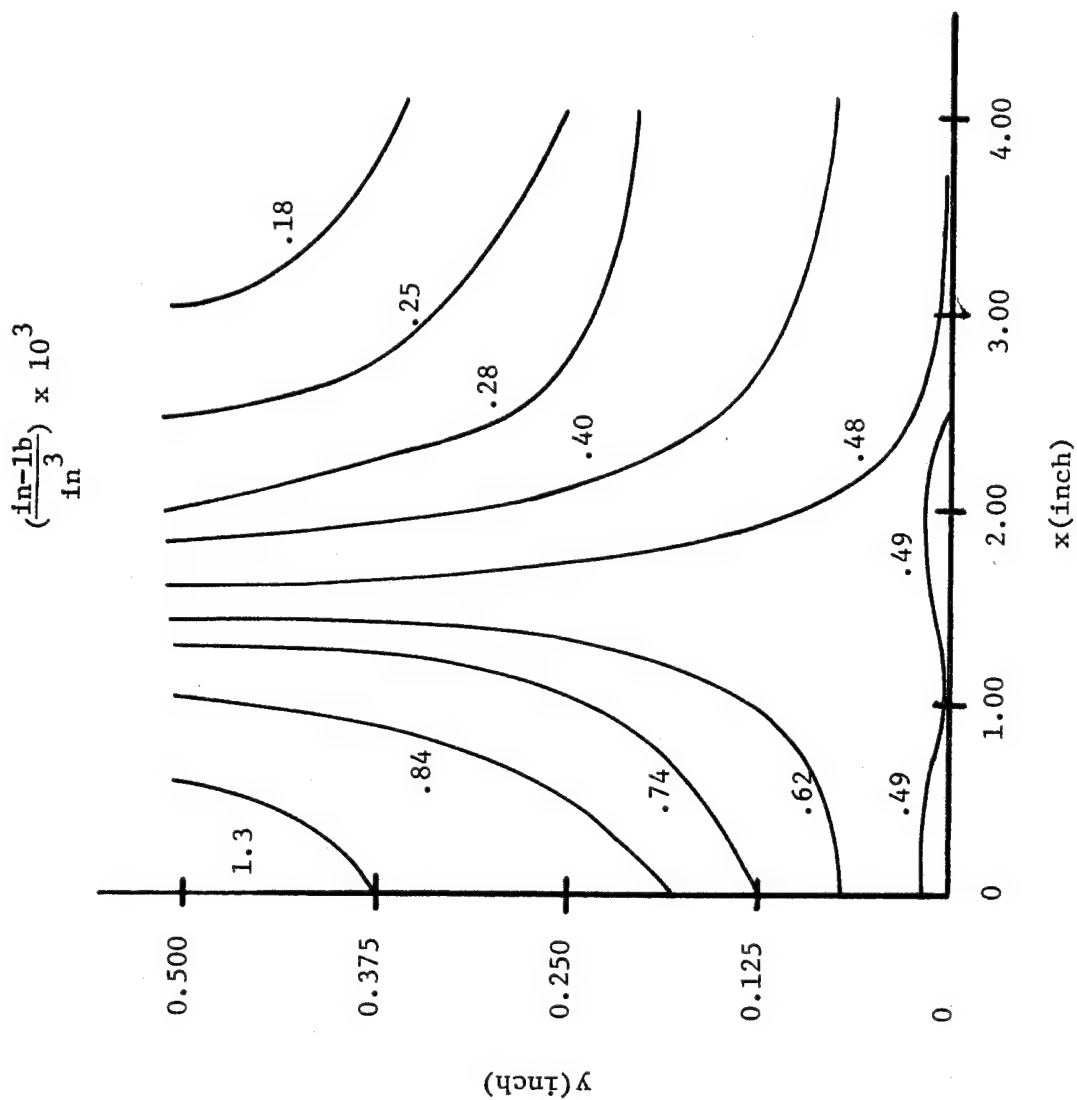


Figure 11. Strain Energy Density Field of [0/+15/0]
Graphite-Epoxy Composite under 10,000 μ -inch
Displacement at $x \approx 2$ -inch.

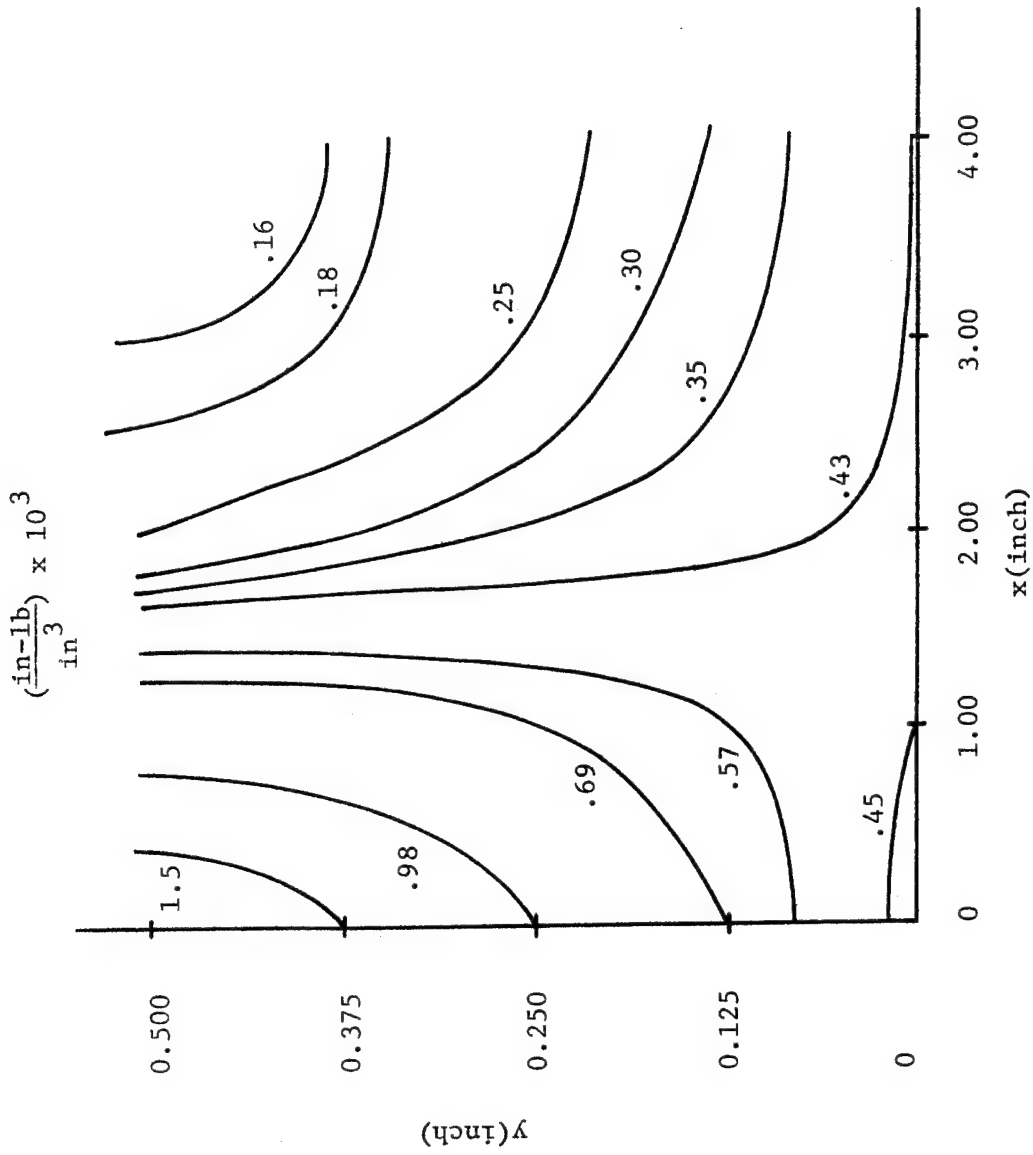


Figure 12. Strain Energy Density Field of [0/±15/0] Graphite-Epoxy Composite under 9,500 μ -inch Displacement at $x = 2$ -inch.

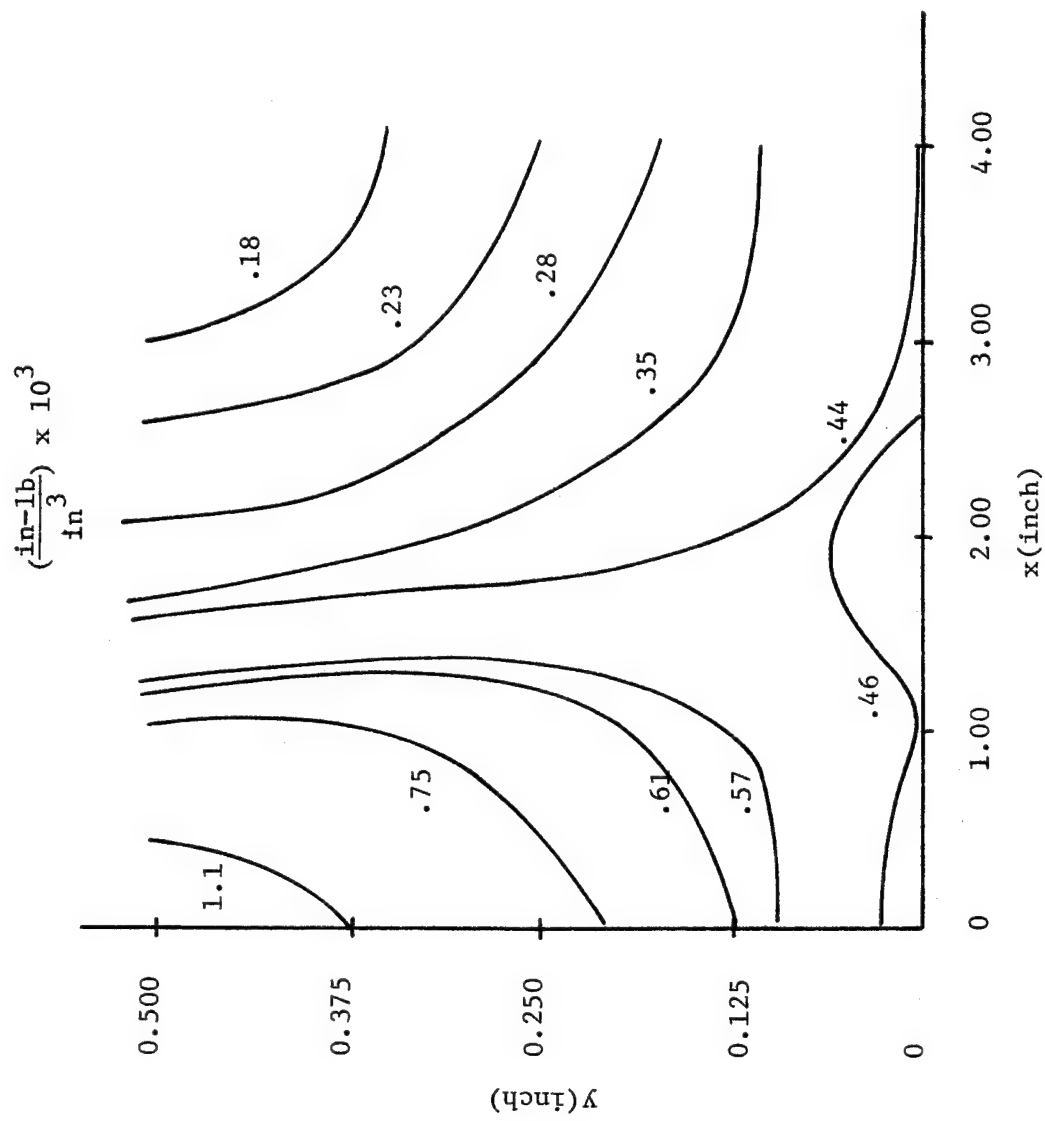


Figure 13. Strain Energy Density Field of [0/+30/0]_s
Graphite-Epoxy Composite under 10,500 μ -inch
Displacement at $x = 2$ -inch

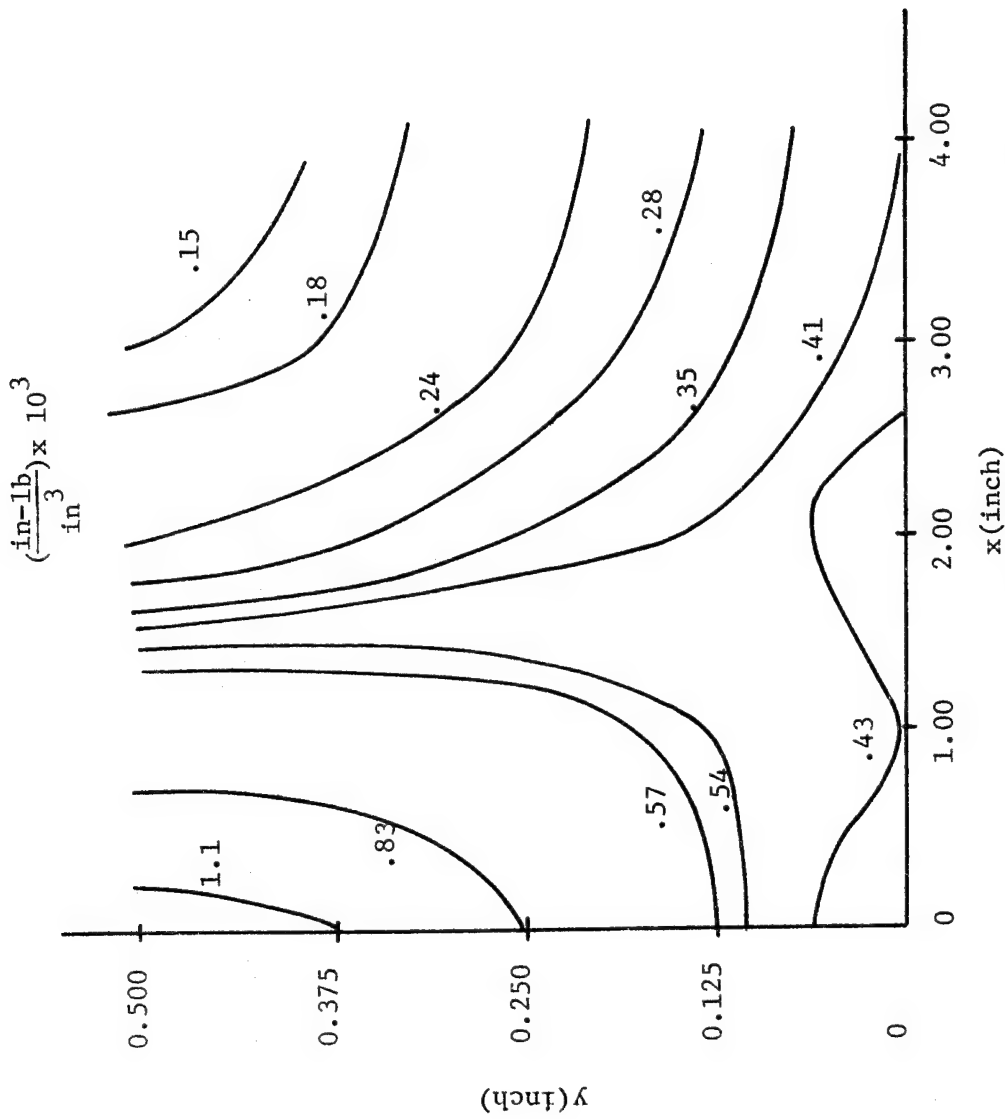


Figure 14. Strain Energy Density Field of $[0/+30/0]_s$ Graphite-Epoxy Composite under $10,000\mu\text{-inch}$ Displacement at $x = 2\text{-inch}$

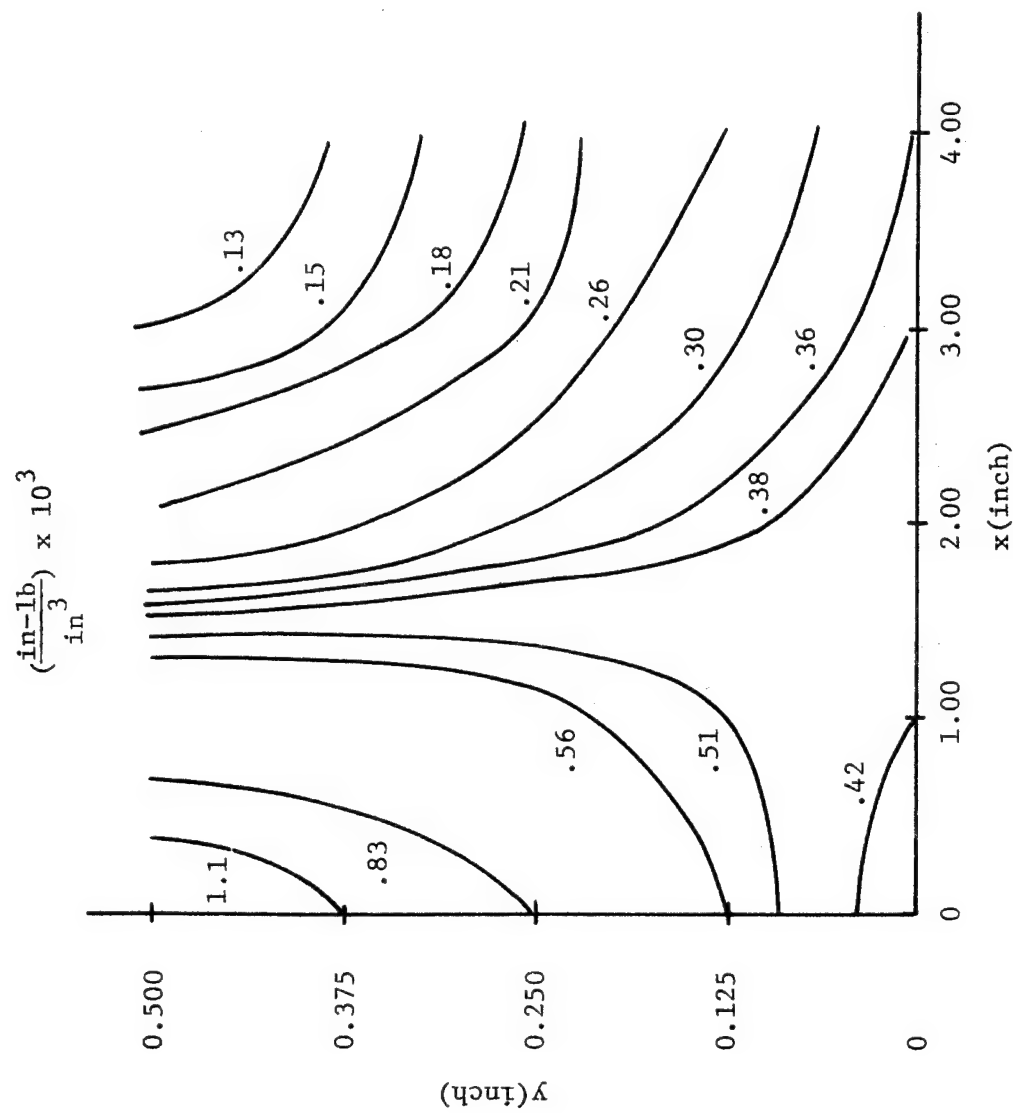


Figure 15. Strain Energy Density Field of $[0/\pm 30/0]_s$ Graphite-Epoxy Composite under 9,500 μ -inch Displacement at $x = 2$ -inch.

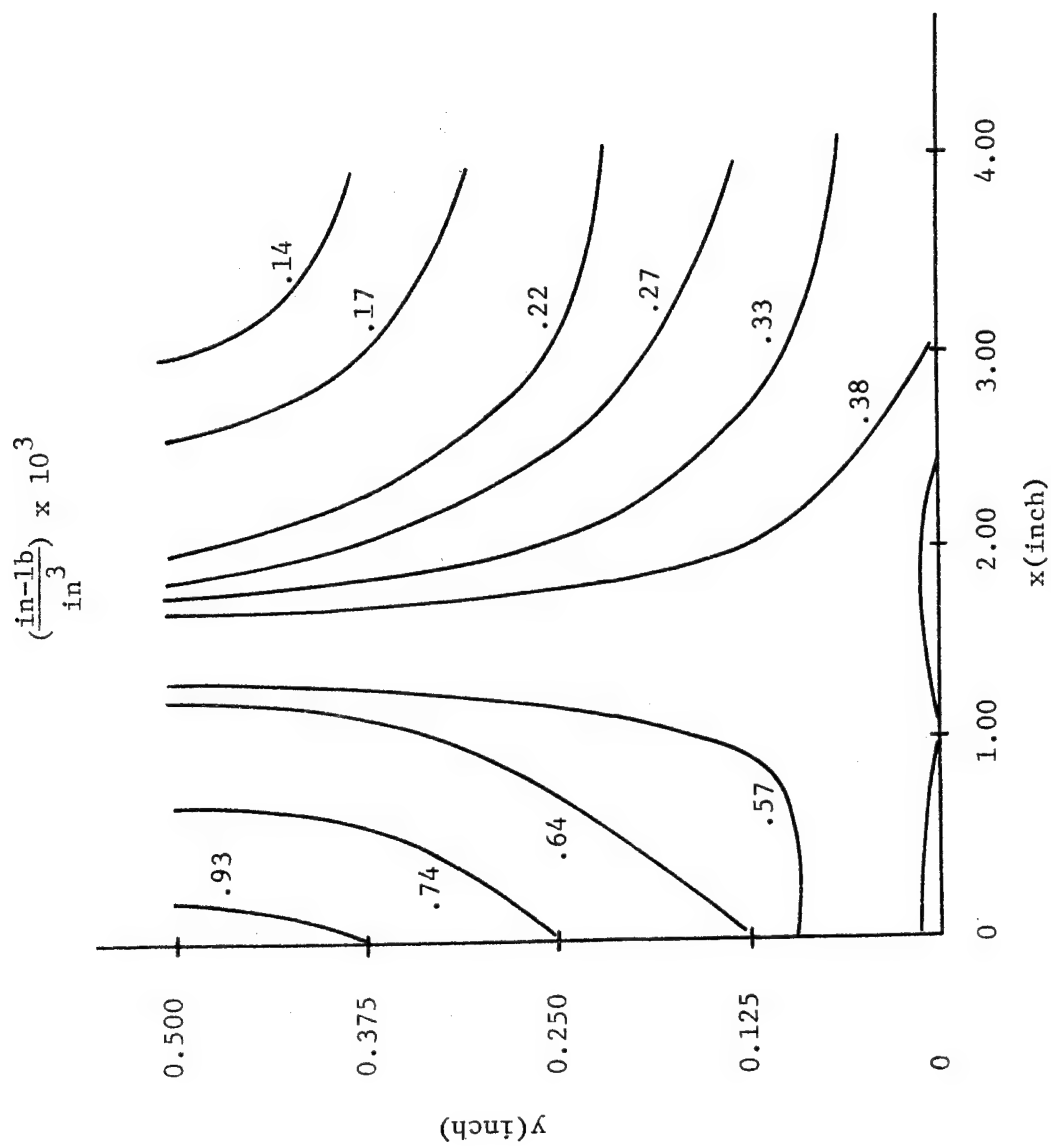


Figure 16. Strain Energy Density Field of $[0/\pm 45/0]_s$ Graphite-Epoxy Composite under $10,500 \mu\text{-inch}$ Displacement at $x = 2\text{-inch}$.

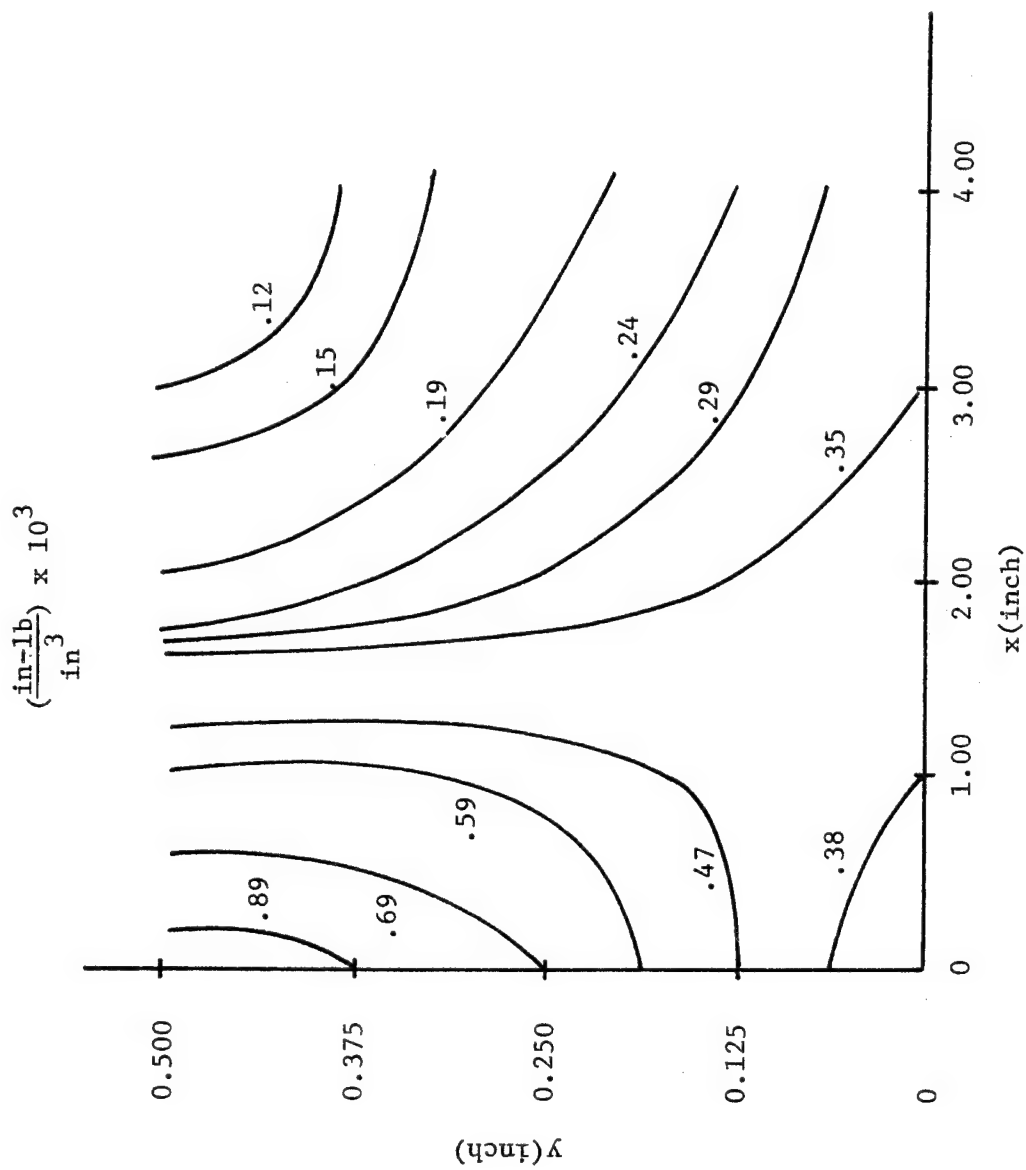


Figure 17. Strain Energy Density Field of $[0/\pm 45/0]_s$ Graphite-Epoxy Composite under 10,000 μ -inch Displacement at $x = 2$ -inch.

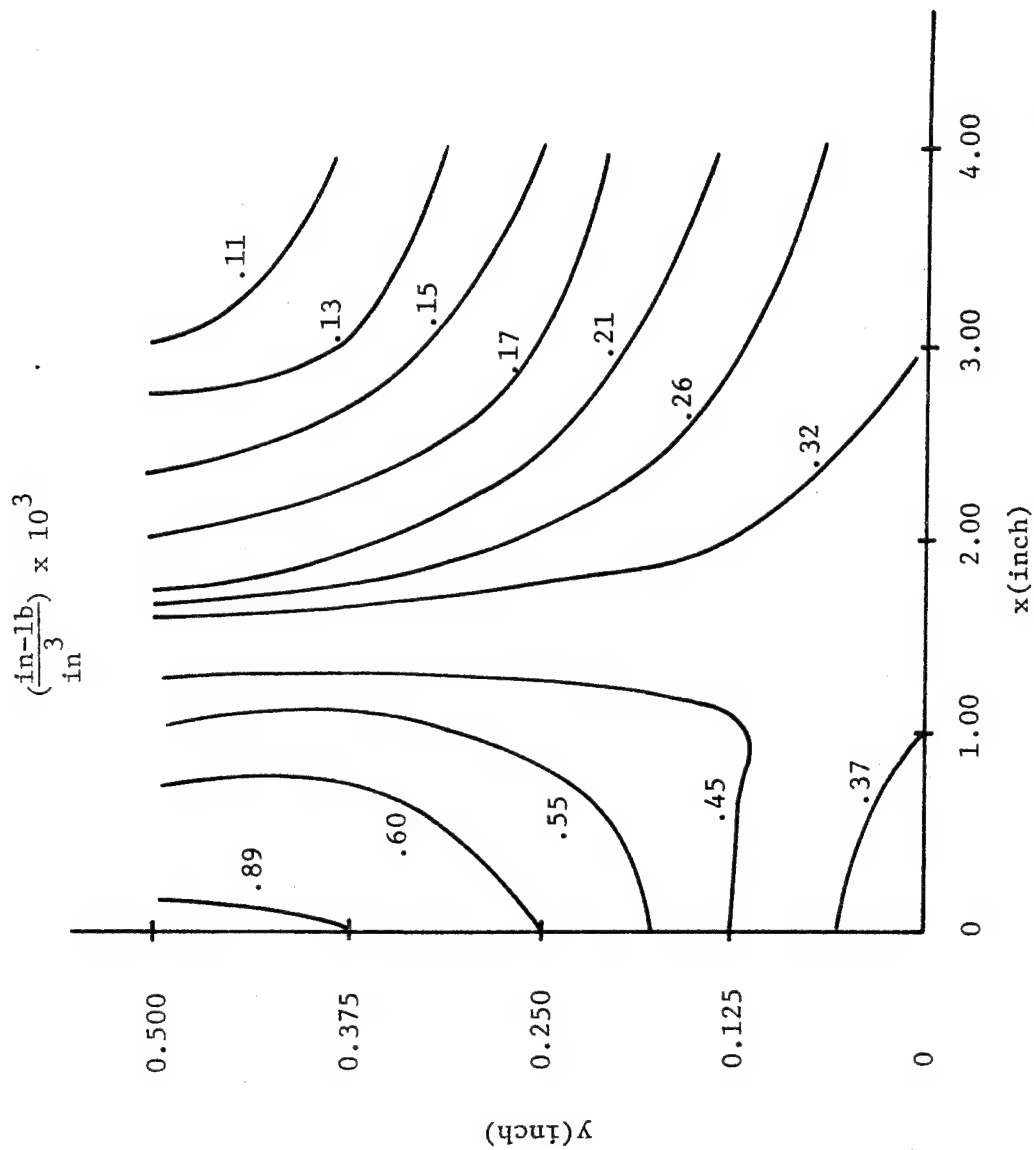


Figure 18. Strain Energy Density Field of [0/±45/0]_s Graphite-Epoxy Composite under 9,500 μ -inch Displacement at $x = 2$ -inch.

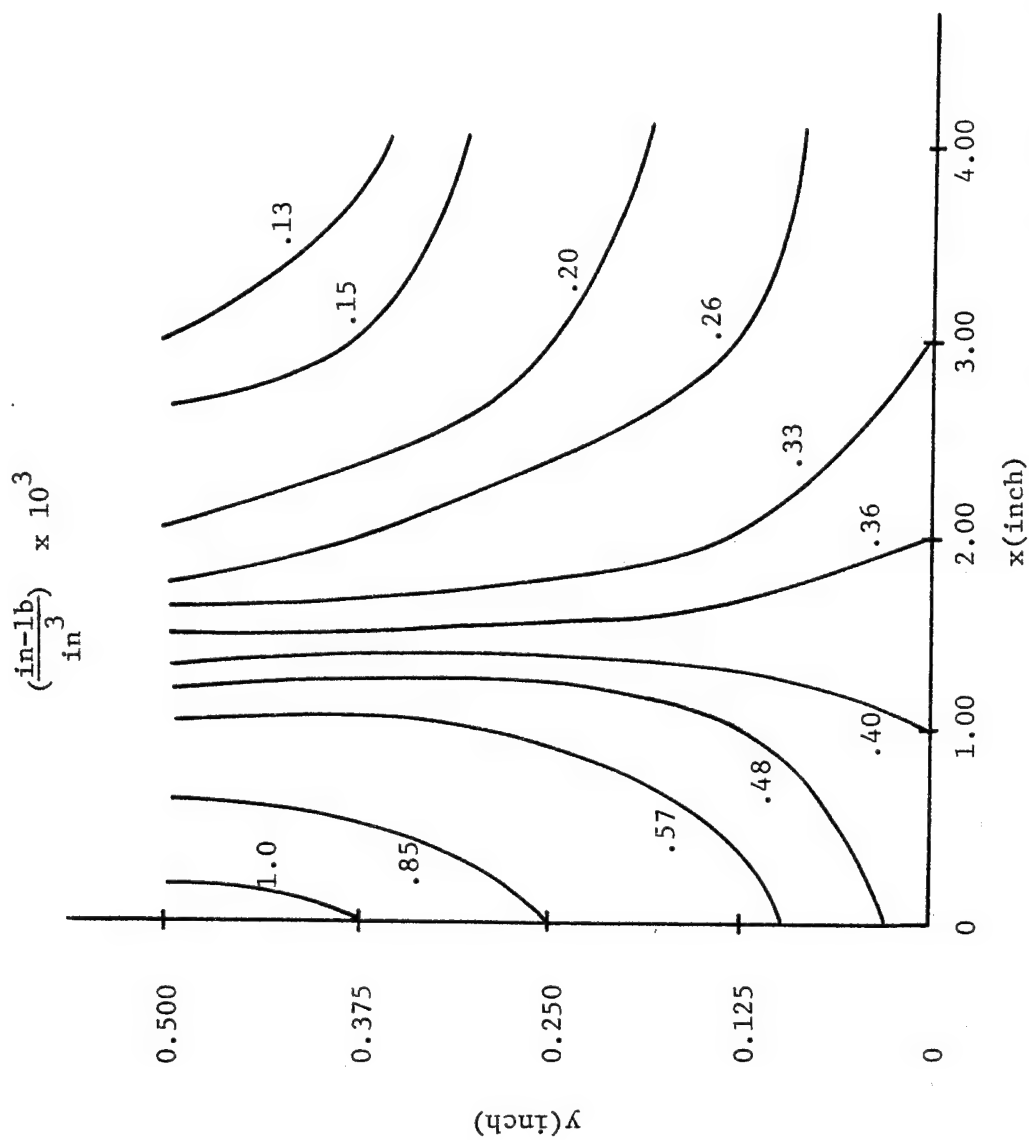


Figure 19. Strain Energy Density Field of $[0/\pm 60/0]_s$ Graphite-Epoxy Composite under 10,500 μ -inch Displacement at $x = 2$ -inch.

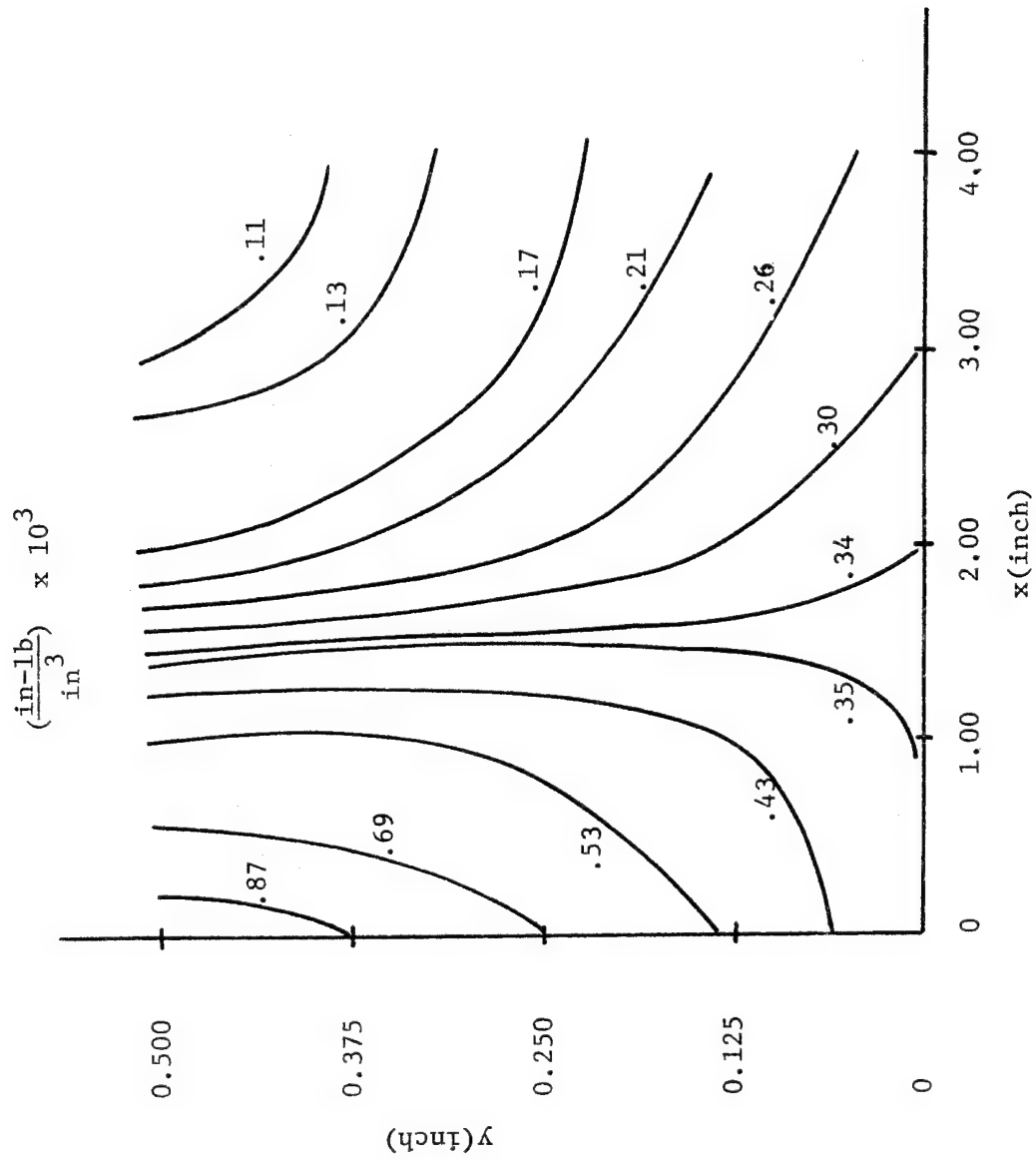


Figure 20. Strain Energy Density Field of $[0/\pm 60/0]_s$ Graphite-Epoxy Composite under 10,000 μ -inch Displacement at $x = 2$ -inch.

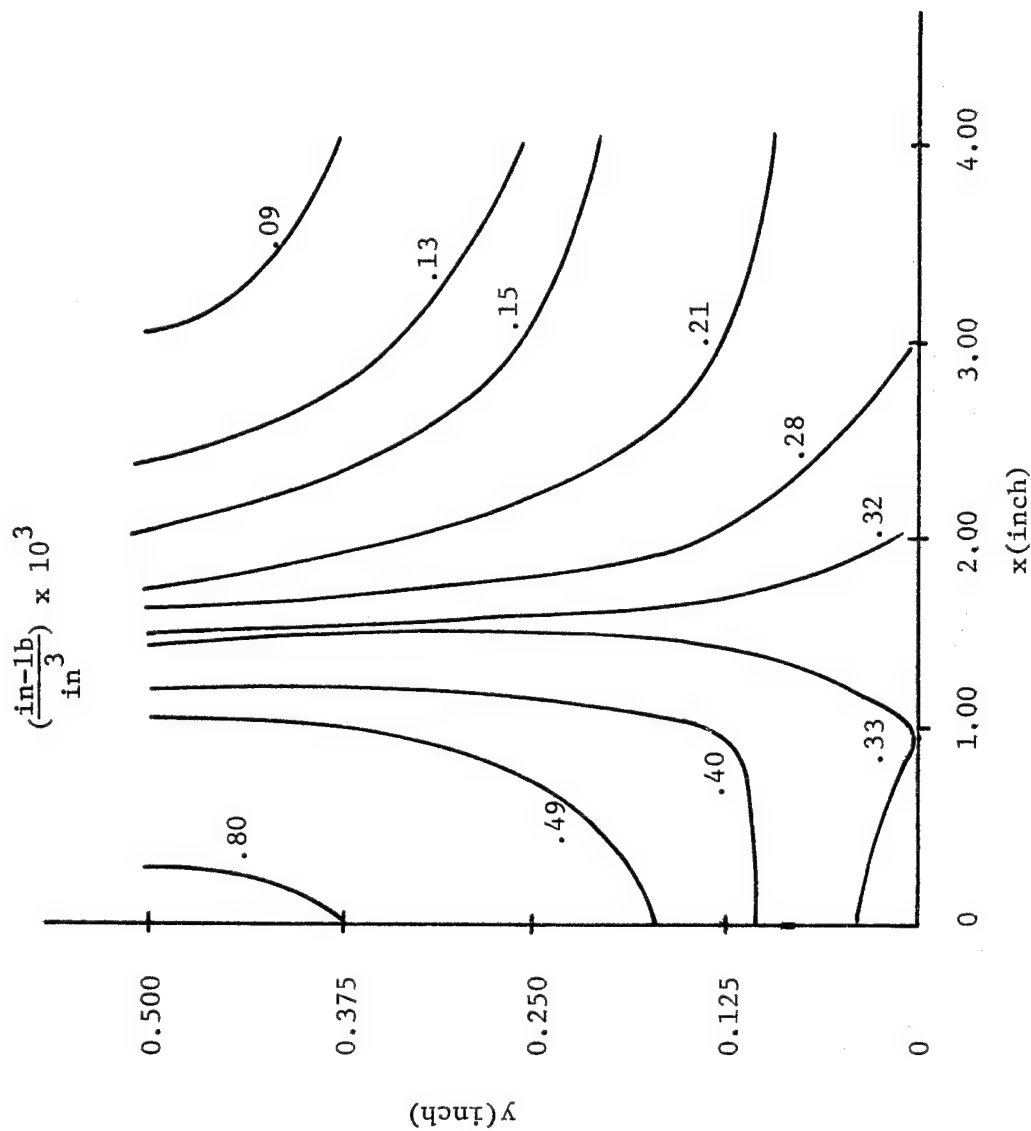


Figure 21. Strain Energy Density Field of $[0/\pm 60/0]_s$ Graphite-Epoxy Composite under 9,500 μ -inch Displacement at $x = 2$ -inch.

4. Static and Dynamic Plate Model With Hole

The field equations (2-5) were converted into finite difference form. There are seven (7) groups of equations that must be considered to solve the problem. They are:

- (1) general field equations
- (2) right boundary conditions
- (3) top boundary conditions
- (4) bottom boundary conditions
- (5) left boundary conditions
- (6) circular hole boundary conditions
- (7) points have close relation with circular boundary

For the explicit method, $(\frac{\Delta \lambda}{\Delta x})^2$ is required to be small enough in order to generate a finite difference solution. Time steps of 2×10^{-5} seconds were required to achieve a reasonable solution.

The grid pattern for the upper right quadrant of the plate is shown in Figure 22. The small grid around the hole was for best definition of the circular boundary conditions. The complication of defining the grid points at the boundary made it difficult to define the strain energy density field or stress concentrations around the hole.

The development of the analysis proved frustrating as the program generated unreasonable data for the grid pattern and boundary conditions used. Another approach is being investigated to minimize the problems generated by the finite difference method.

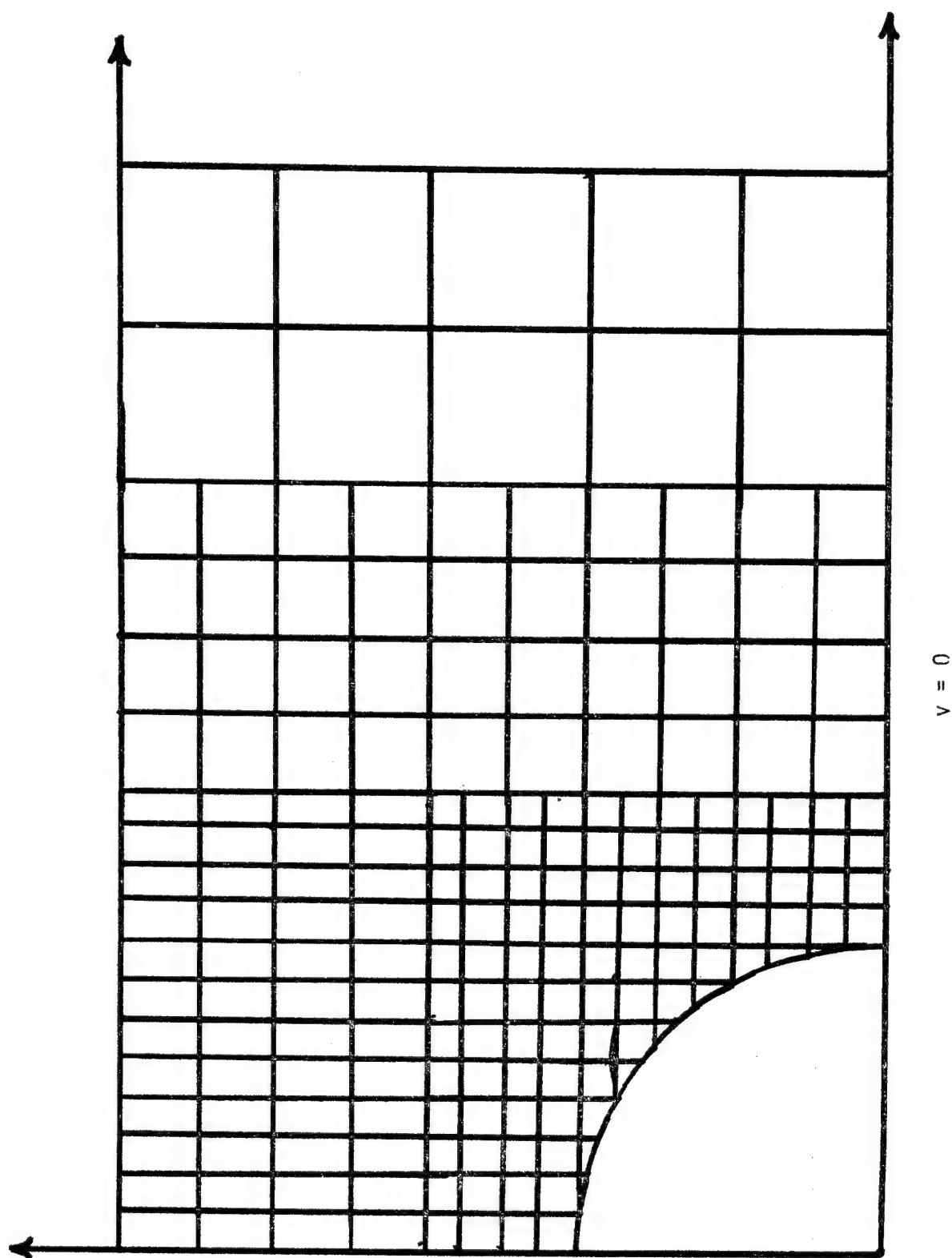


Figure 22. Grid Pattern for Analysis of Composite Plate with Hole.

$$0 = n$$

SECTION IV

EXPERIMENTAL DATA

The graphite-epoxy system, with general fiber orientation $[0/\pm\theta/0]_s$, was subjected to tensile static fatigue. The test specimen geometries were shown in Figure 1. The static specimens were strain gaged with EA-09-062TT-120 gages. These gages provide the monitoring of both longitudinal and transverse deformations. The strain gaged specimens were placed in an Instron test machine and deformed at 0.02 inch/minute. The constant crosshead movement provides determination and comparison of elastic behavior.

The graphite-epoxy fatigue specimens, with 3/16-inch diameter hole, were subjected to tensile cyclic loading. A Gilmore Universal Testing System was used to apply a sinusoidal load function to the specimens under constant load conditions. The tensile fatigue tests were tension (S_{max}) - 0 - tension (S_{max}). The minimum tensile stress (S_{min}) was not zero but slightly in tension to avoid microbuckling from compressive loading. The value of R was equal to 0.005 in all tests ($R = S_{min}/S_{max}$). The fatigue specimens were subjected to 3 loading conditions (55%, 62.5%, and 70% of static ultimate tensile stress) and 2 frequencies (3 and 25 Hertz). The loading conditions were based on static specimen geometry. The 3/16-inch diameter holes were not considered when calculating the cross-sectional areas. The specimens were allowed to be tested until failure occurred or 10^6 cycles were attained. The tensile fatigue data provided an insight to the failure mechanism.

The test specimens, tensile static and fatigue, were examined following fracture in order to note the failure surfaces.

1. Graphite-Epoxy Composite

The tensile static and dynamic test specimens were supplied by the Air Force Flight Dynamics Laboratory. Thornel 300 graphite yarn was the fiber combined with 5208 epoxy resin. The properties of Thornell 30 [31] are contained in Table 1. The Thornel 300/5208 composite flat plate

Table 1. Properties of Thornel 300 Graphite Yarn

Property	Unit	Value
tensile strength	lb/in ²	360,000
tensile modulus	lb/in ²	34 x 10 ⁶
density	g/cc	1.76
elongation at break	%	1

specimens were autoclave cured (Whittacker Corp. specification) and post cured for 4 hours at 400°F. The individual constituents within the laminates are summarized in Table 2.

Table 2. Content of Thornel 300/5208 Laminates

Fiber Orientation	Specimen Letter	v/O Fiber	v/O Resin	v/O Void
[0/+0/0] _s	A	68.3	30.4	1.3
[0/+15/0] _s	B	65.1	33.8	1.1
[0/+30/0] _s	C	66.8	32.1	1.1
[0/+45/0] _s	D	66.9	31.5	1.6
[0/+60/0] _s	E	65.2	33.3	1.5

The laminates vary from 65.1 to 68.3 in fiber volume percent. This variation is small so the test results of the laminates can be compared.

The fabrication of theThornel 300/5208 laminates was of high quality; which is basic to a test program.

2. Static Test Results

Two each of the $[0]_g$ (A) and $[0/\pm 15/0]_s$ (B) static test specimens were subjected to uniaxial tensile loading. Strain gages were placed on each flat surface of the test specimen. Differentials in strain gage readings would indicate bending in the specimen. The average of the two gages on each specimen was used to produce the stress-strain curve. The stress-strain relationships for these fiber orientations are shown in Figures 23 and 24.

Two each of the $[0/\pm 30/0]_s$ (C), $[0/\pm 45/0]_s$ (D), and $[0/\pm 60/0]_s$ (E) static test specimens were subjected to uniaxial tensile loading. One strain gage was placed on the flat surface of each test specimen for monitoring longitudinal and transverse deformations. The stress-strain relationships for these fiber orientations are shown in Figures 25, 26 and 27.

The mechanical properties of the $[0/\pm \theta/0]_s$ Thornel 300/5208 composite specimens are summarized in Table 3. The data recorded are

Table 3. Mechanical Properties of Thornel 300/5208 Composite Specimens

Property	$[0]_g$ A	$[0/\pm 15/0]_s$ B	$[0/\pm 30/0]_s$ C	$[0/\pm 45/0]_s$ D	$[0/\pm 60/0]_s$ E
F_{tu} (psi)	227,000	155,480	139,910	116,790	100,360
ϵ_{tu} (μ -in/in)	9830	7711	9610	8710	8540
E_T (10^6 psi)	21.9	19.3	15.4	12.5	11.8
ν	0.29	0.64	0.98	0.65	0.27
F_{pg} (psi)			96,500	82,000	

the average of two specimens per fiber orientation.

The mechanical properties generated with the static test specimens were used in tensile fatigue testing.

3. Tensile Fatigue Results

Tensile fatigue data were generated for the Thornel 300/5208 composites using a sinusoidal loading function under constant load conditions. Three loading conditions and two frequencies were used. The S_{max} used was 55%, 62.5%, and 70% of tensile ultimate stress determined by static test and these static test specimens were used as control specimens.

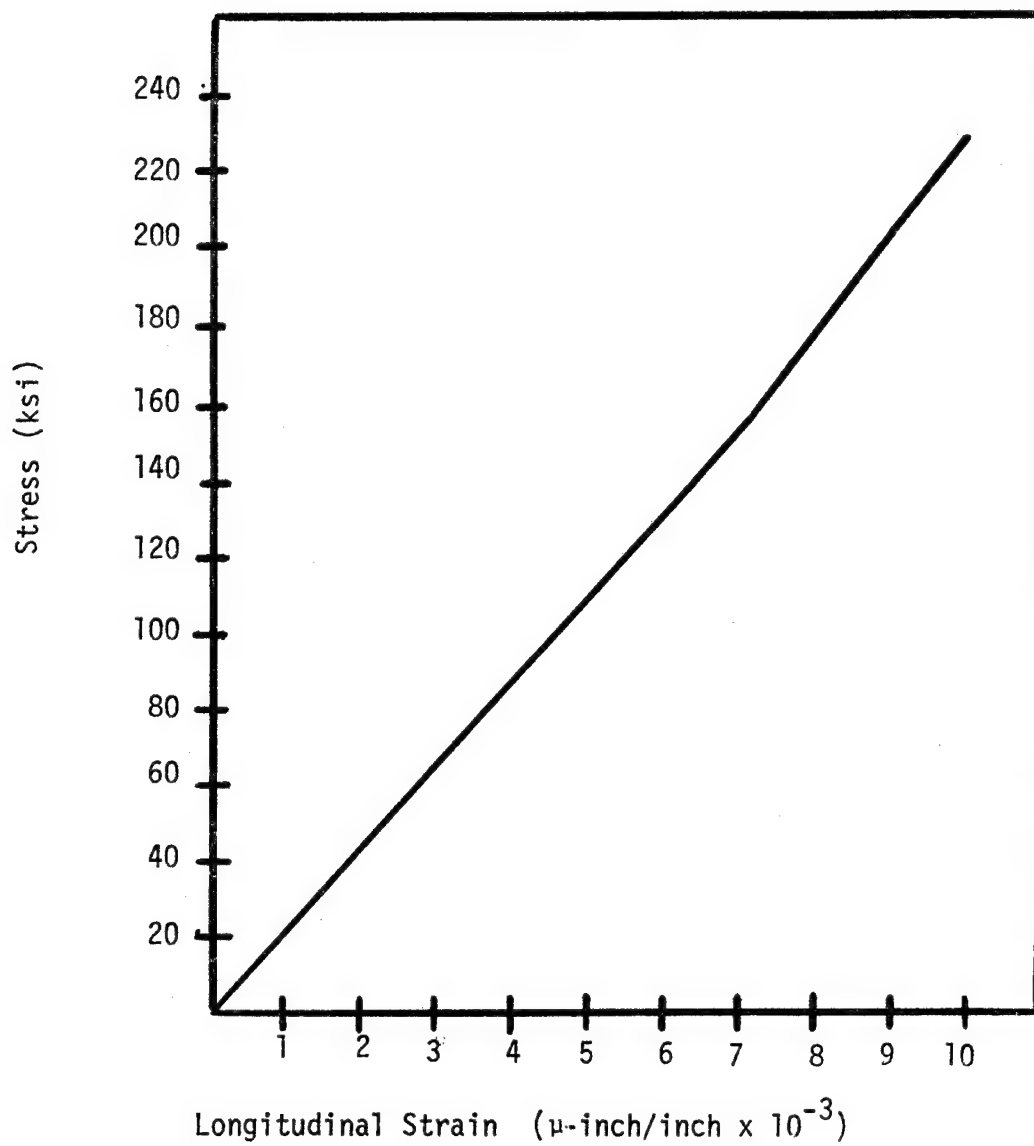


Figure 24. Stress-Strain Curve for [0]_g Thorne1
300/5208 Composite

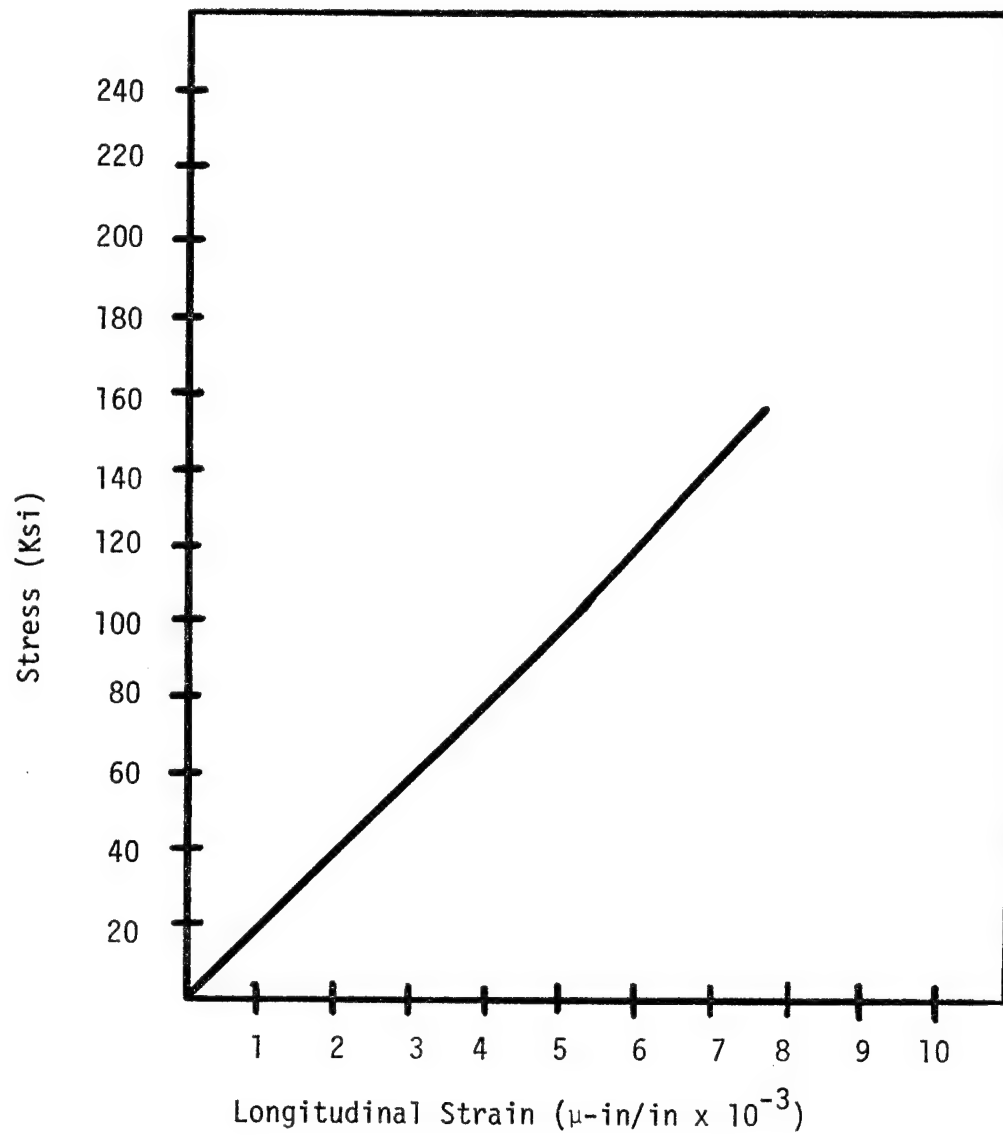


Figure 24. Stress-Strain Curve for $[0/\pm 15/0]_s$ Thorne1 300/5208 Composite.

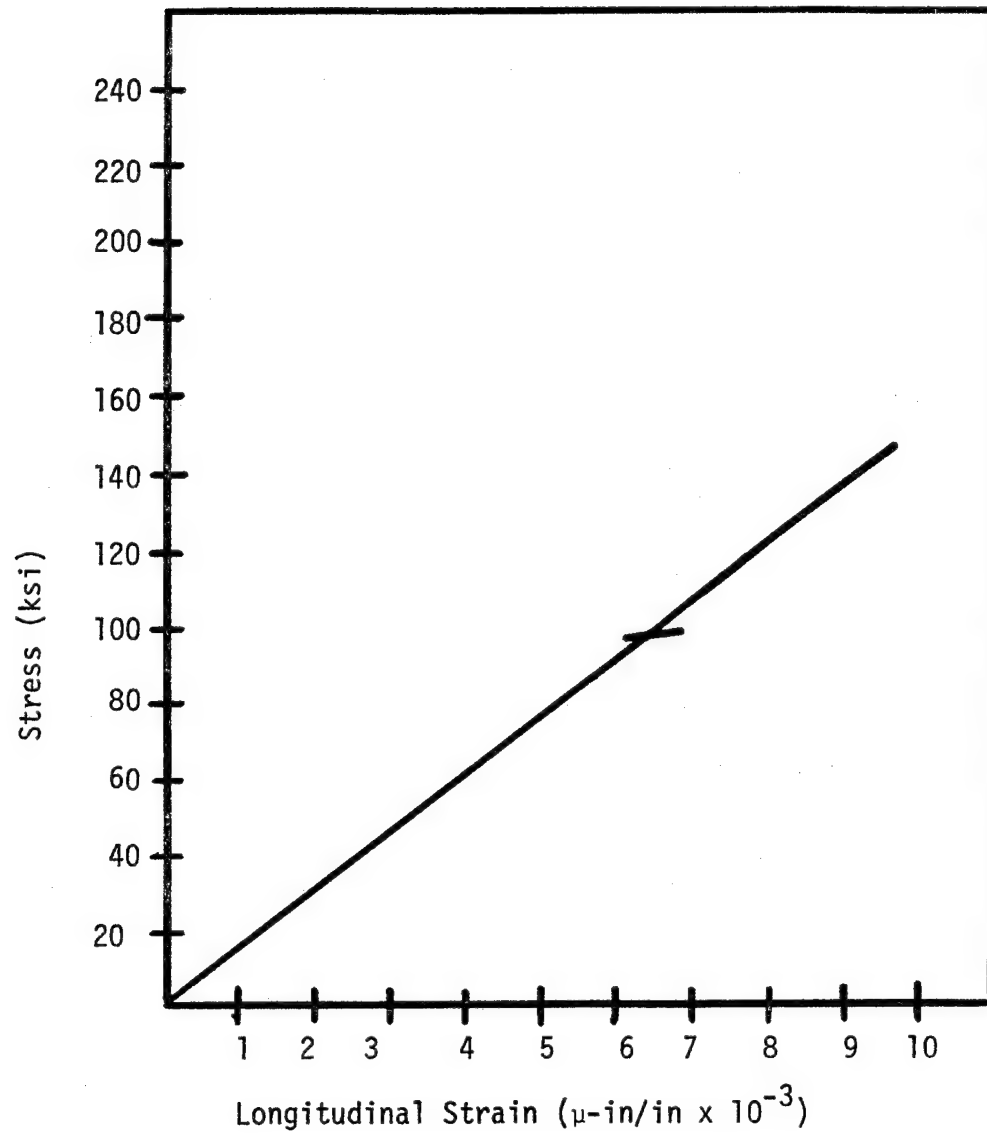


Figure 29. Stress-Strain Curve for $[0/\pm 30/0]_S$ Thorne1 300/5208 Composite.

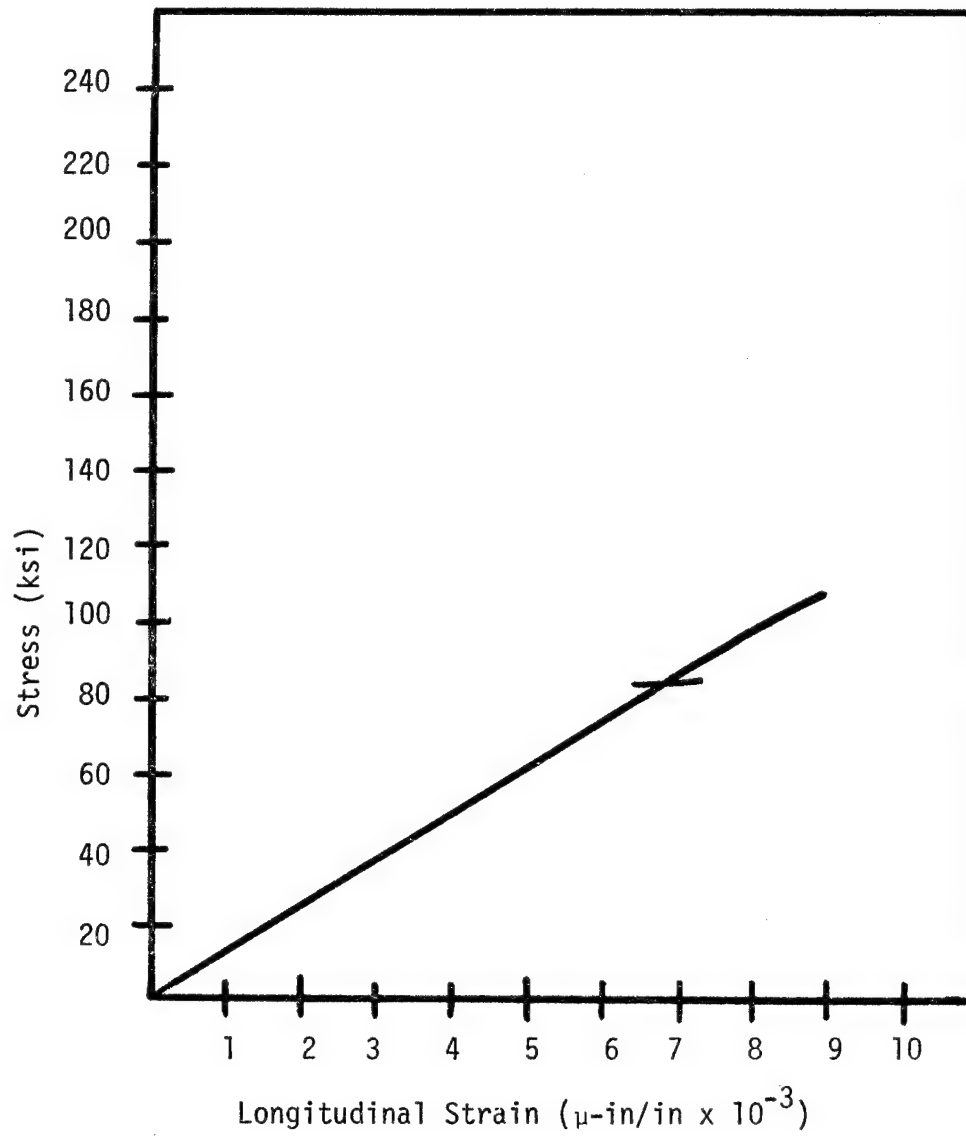


Figure 26.. Stress-Strain Curve for $[0/+45/0]_s$ Thorne1 300/5208 Composite.

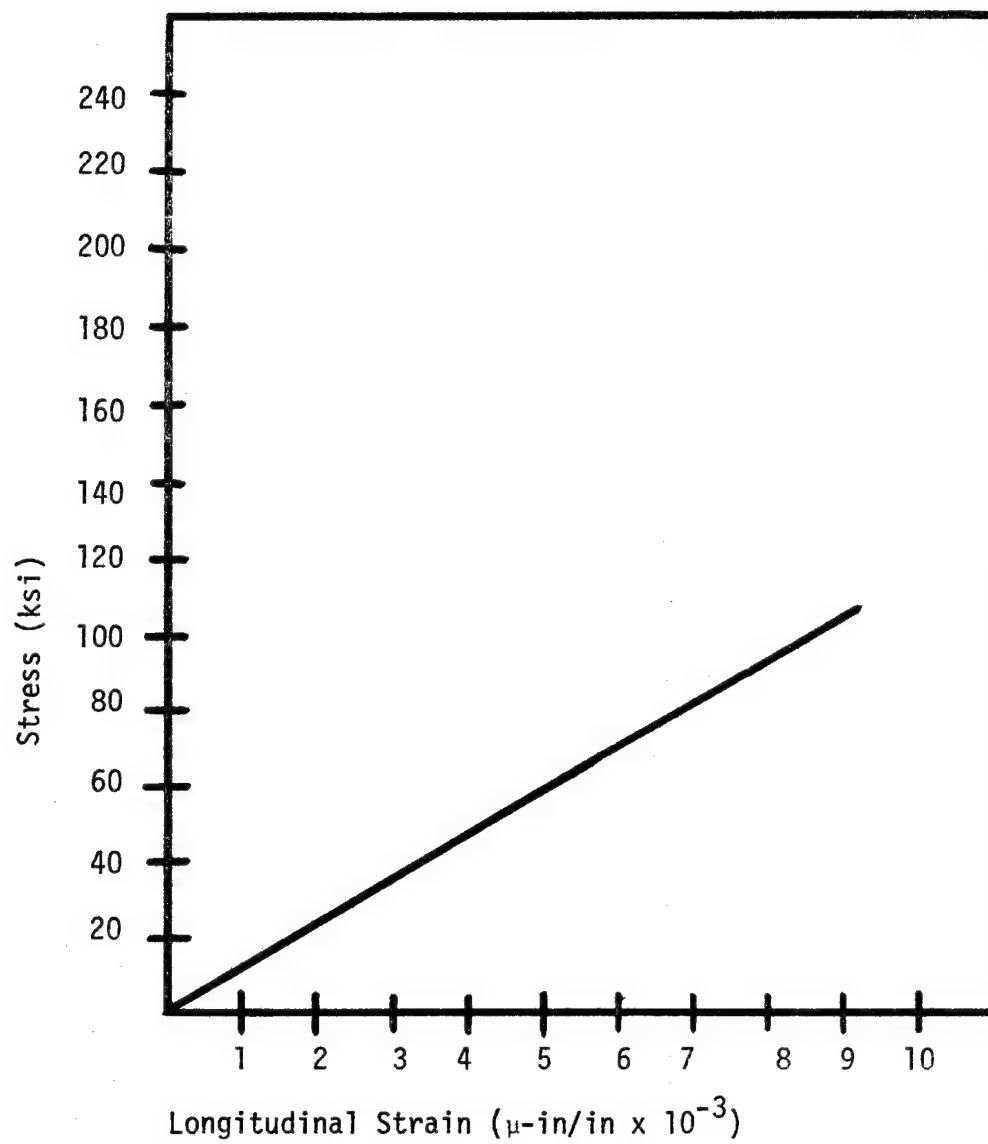


Figure 27. Stress-Strain Curve for $[0/+60/0]_s$ Thornel 300/5208 Composite.

The applied stress considered the plate without a circular hole. The maximum alternating stresses for the various geometries are given in Table 4. The stresses were obtained from no hole specimens and applied to specimens with hole. The value of R was equal to 0.005. The specimens were submitted to

Table 4. Maximum Alternating Stresses Used in Tensile Fatigue Testing (No Hole)

Property	$[0/\pm 0/0]_s$ A	$[0/\pm 15/0]_s$ B	$[0/\pm 30/0]_s$ C	$[0/\pm 45/0]_s$ D	$[0/\pm 60/0]_s$ E
F_{tu} (psi)	227,000	155,480	139,910	116,790	100,360
S_{max} (psi)					
70% F_{tu}	157,000	108,000	96,500	82,000	68,000
62.5% F_{tu}	141,300	97,200	86,850	73,800	61,200
55% F_{tu}	125,600	86,400	77,200	65,600	54,400

constant load conditions at 3 and 25 Hertz. The results of the tensile fatigue testing are shown in Figures 28 through 32. The ultimate tensile strength of the static specimen without holes is noted on the plots. The test was completed when either failure occurred or 10^6 cycles were obtained. Two (2) specimens were tested per condition. As a result, no statistical evaluation of the data is possible. However, the limited data do indicate trends.

The damage indicated by cyclic loading, as compared to static loading is less for the D and E configurations. This relates directly to the stress concentrations present at the periphery of the hole. The life (number of cycles to failure) was less for low-frequency fatigue specimens (3 Hertz) than the high-frequency fatigue specimens (25 Hertz). All high-frequency fatigue specimens attained 10^6 cycles with a S_{max} of 55% F_{tu} . The low-frequency

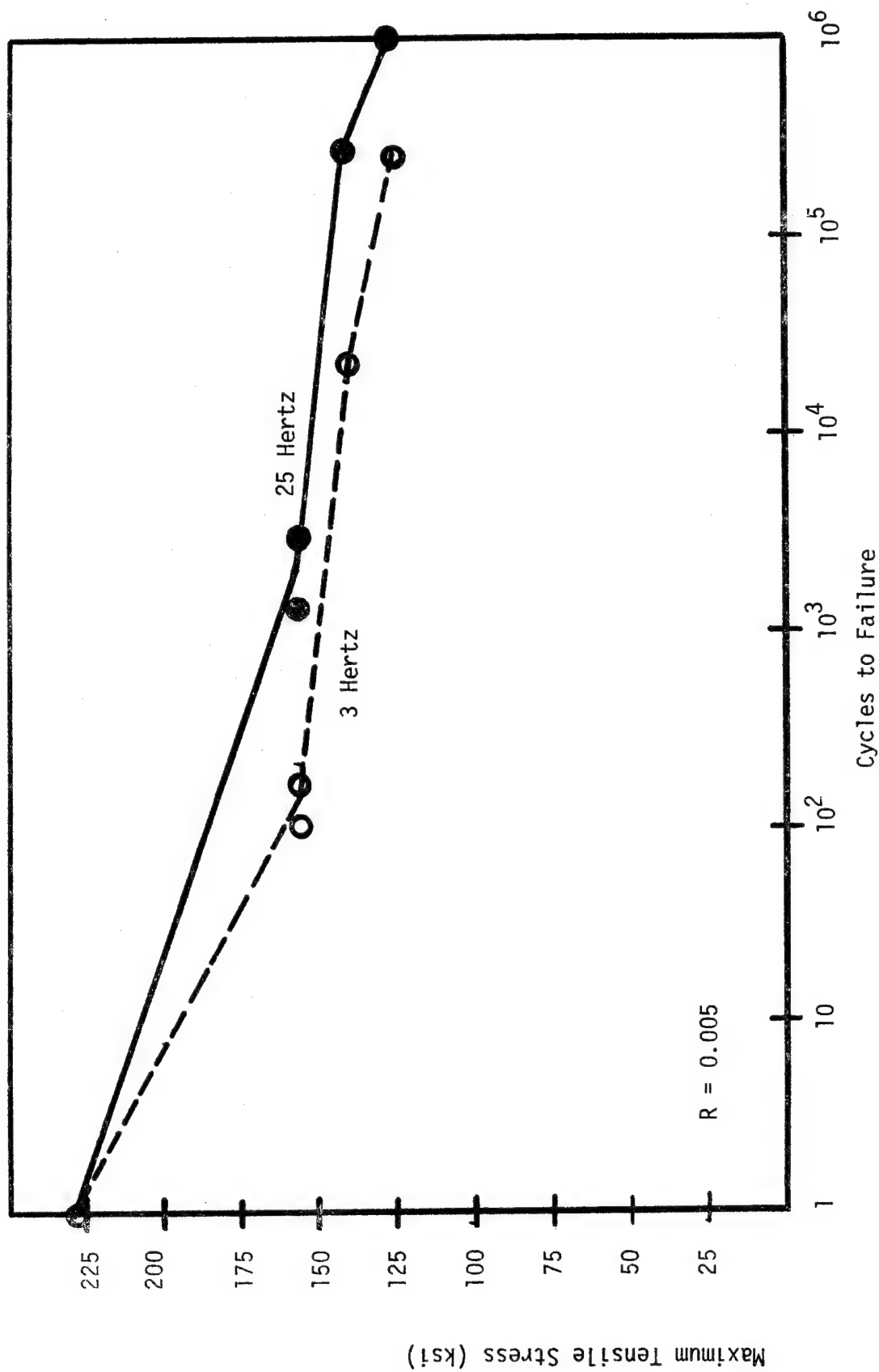


Figure 28. Tensile Fatigue Curve for [0]_g Thornel 300/5208 Composite

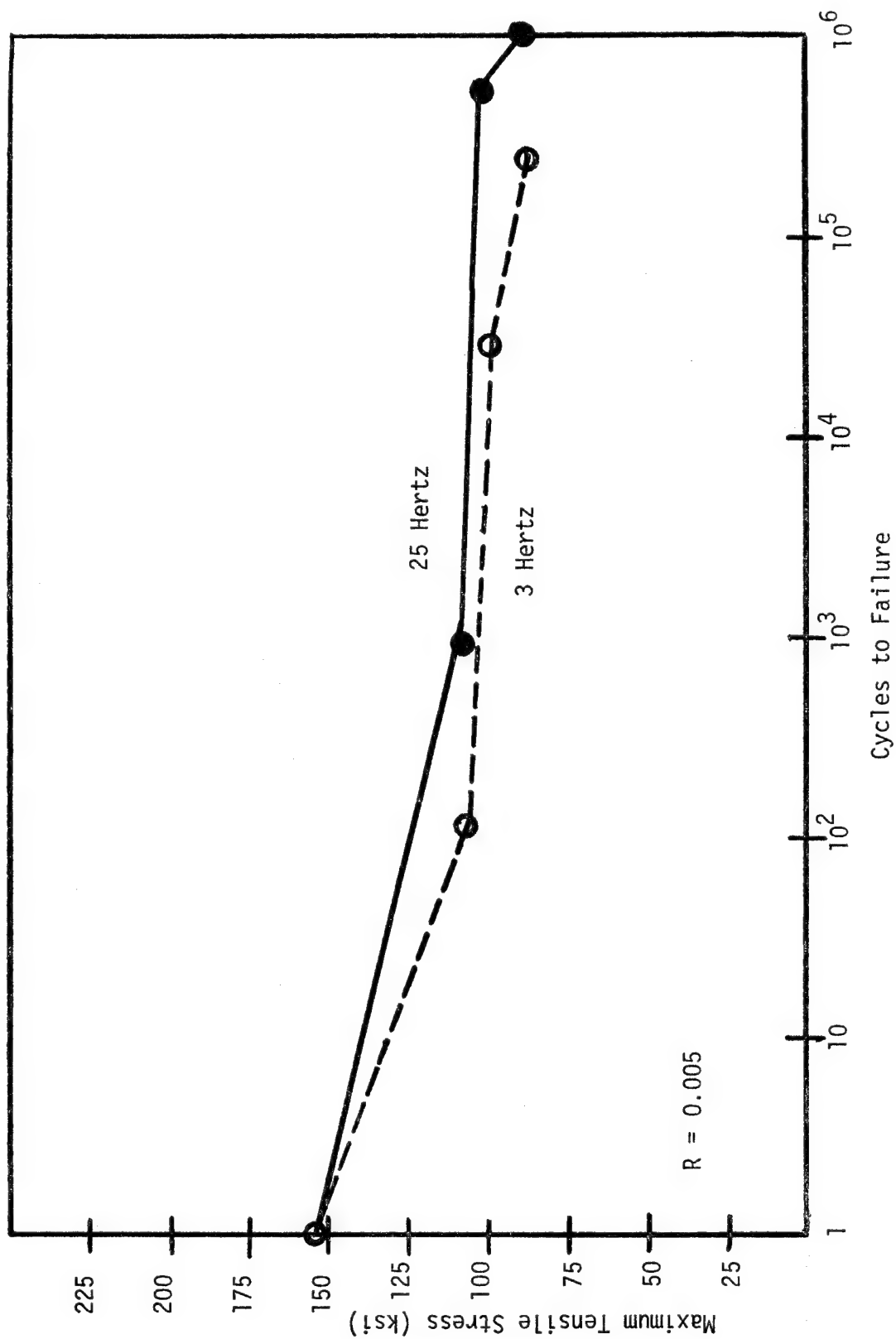


Figure 29. Tensile Fatigue Curve for [0/+15/0]_s Thorne1 300/5208 Composite.

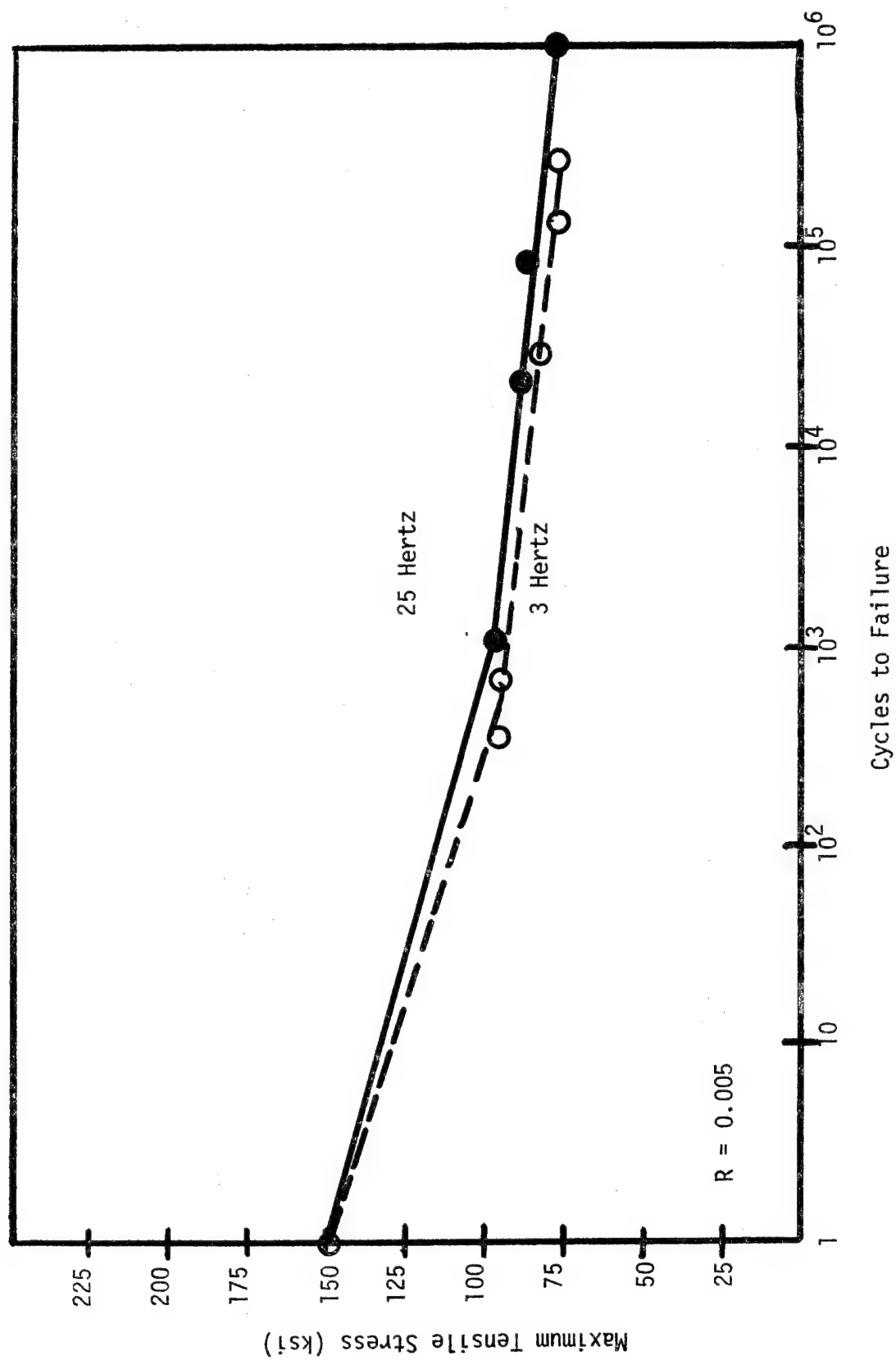


Figure 30. Tensile Fatigue Curve for $[0/+30/0]_s$ Thorne1 300/5208 Composite.

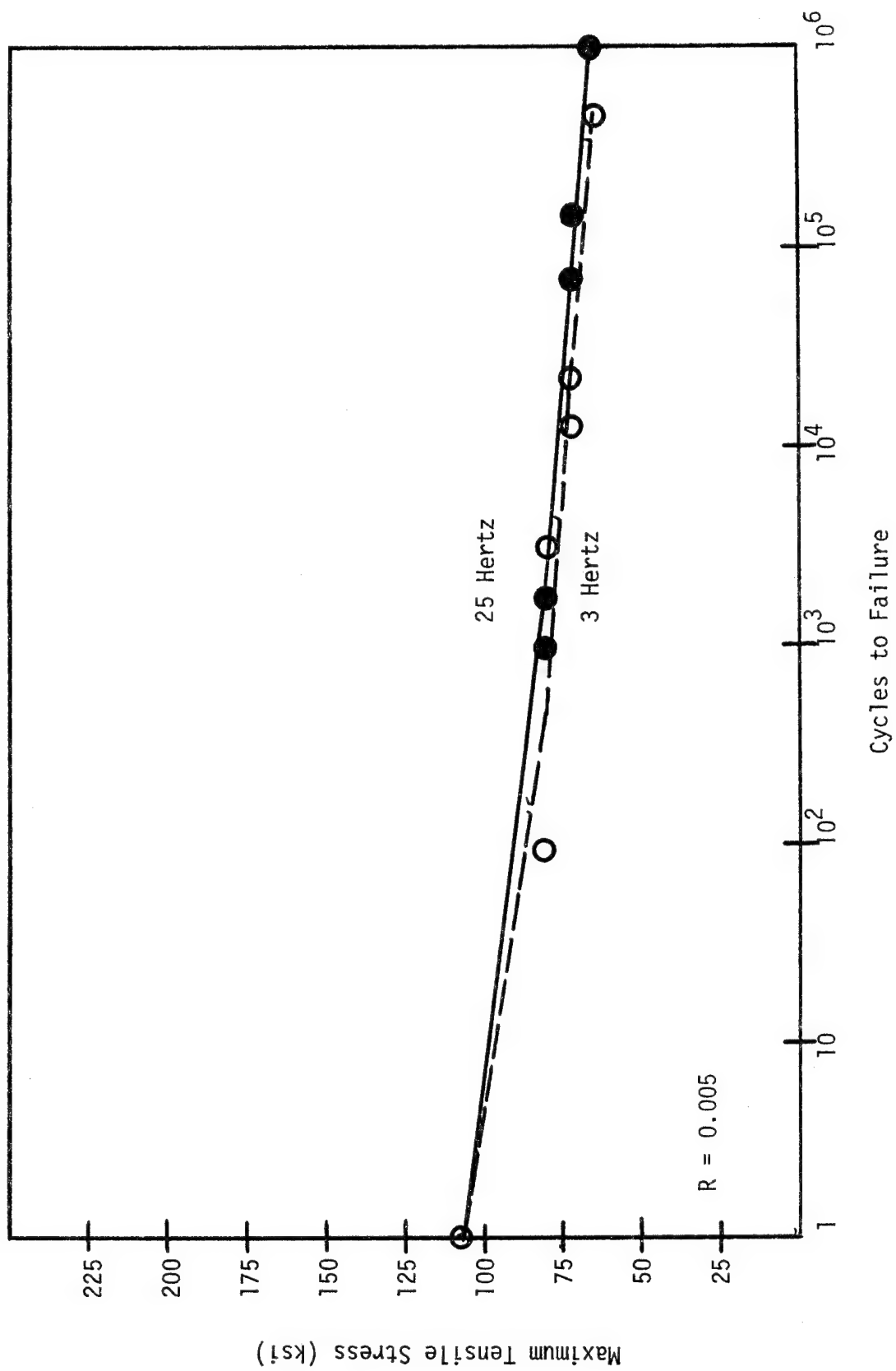


Figure 31. Tensile Fatigue Curve for $[0/+45/0]_s$ Thorne1 300/5208 Composite.

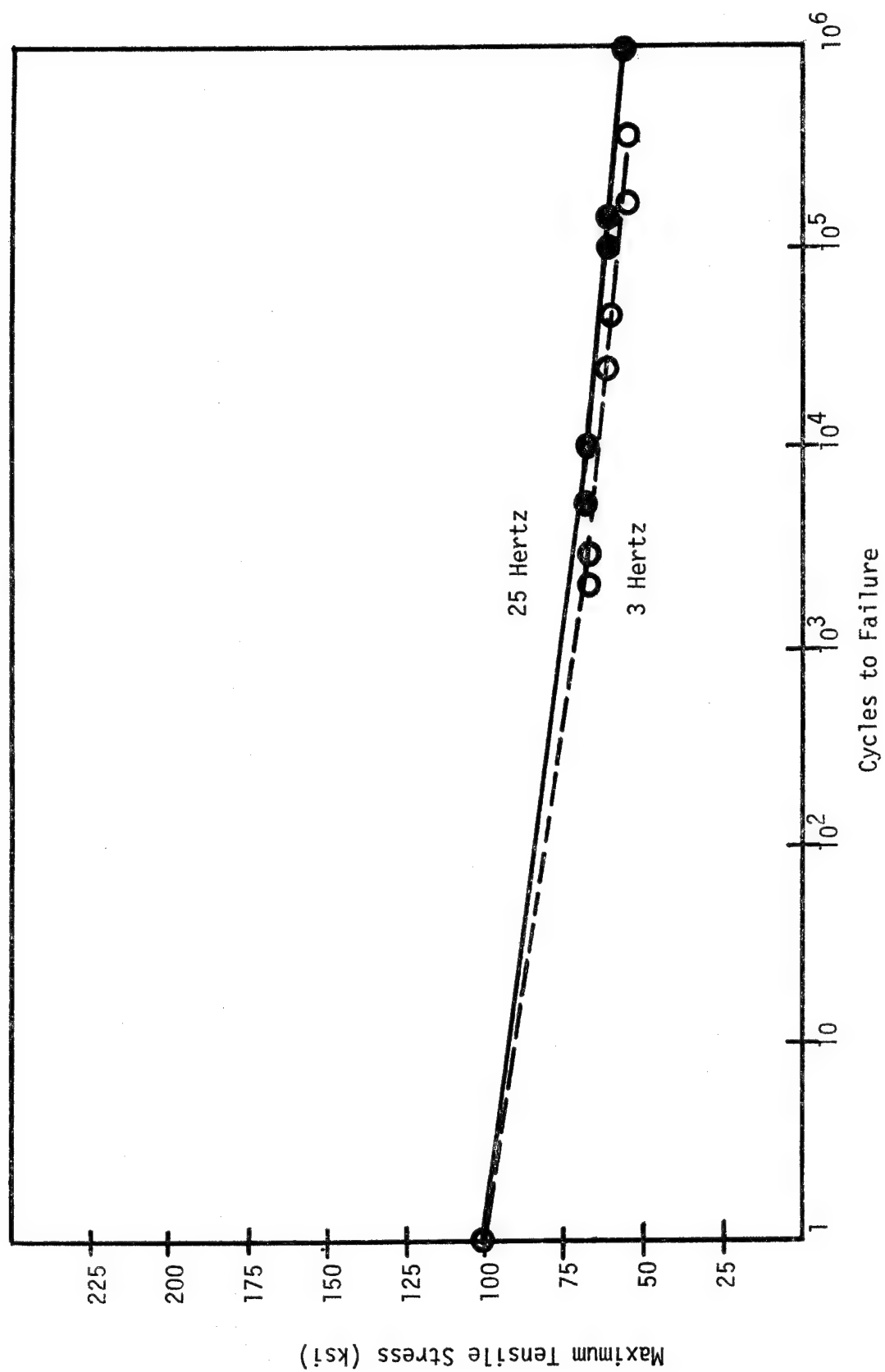


Figure 32. Tensile Fatigue Curve for $[0/+60/0]_s$ Thorne1 300/5208 Composite.

fatigue specimens all failed, even under the low S_{\max} .

The damage mechanisms occurring within the composites appear to be related to frequency (time) and level of loading. However, the mechanisms appear to be of similar type.

4. Test Specimen Failure

The tensile static and fatigue test specimens were observed during test and following fracture to note mode of failure. Test specimen notation was used for identification by AFFDL. Fractured static test specimens are shown in Figures 33 through 35. The tensile fatigue specimens are shown in Figures 36-45.

The static specimens reached a maximum load or deformation and fractured suddenly. The unidirectional specimens splintered while fibers broke. The B specimens fractured along the $\pm 15^\circ$ fiber orientation. The specimens containing $\pm 30^\circ$ and $\pm 45^\circ$ plies fractured almost in a straight line across the width. The specimen with $\pm 60^\circ$ plies fractured near the grip at the $\pm 60^\circ$ angle.

The tensile fatigue specimens exhibited secondary as well as primary modes of failure. Fiber breakage was observed in all tensile fatigue tests. Separation of portions of the specimen from the grips was noted in many cases. Delamination of portions of the surface plies was observed in C, D, and E specimens. This is related to Poisson's effect. Fiber breakage and delamination was observed on the edge of all specimens. All of these failure modes are considered secondary.

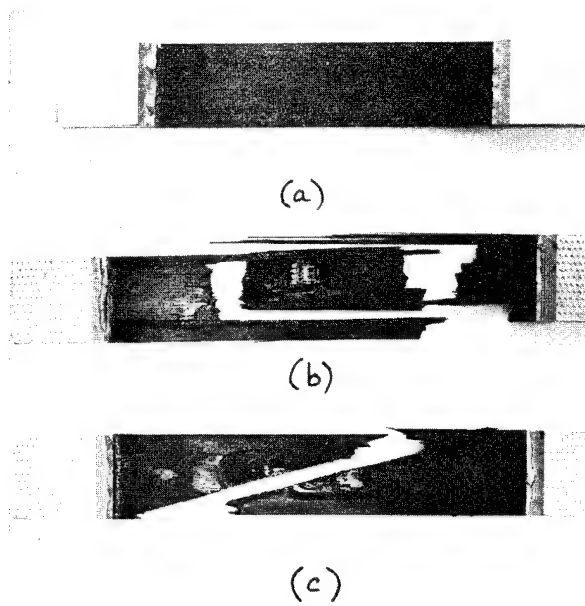


Figure 33. Static Test Specimens:
 (a) Static Specimen, (b) A-1-30, (c) B-1-11.

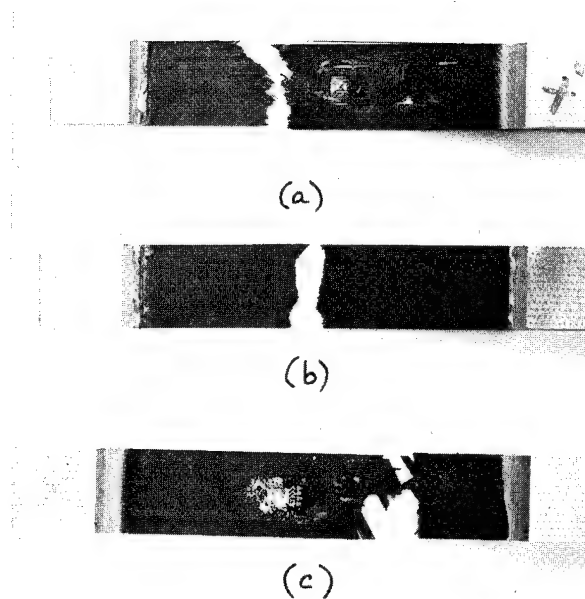


Figure 34. Static Test Specimens:
 (a) C-1-17, (b) D-1-7, (c) E-1-34.

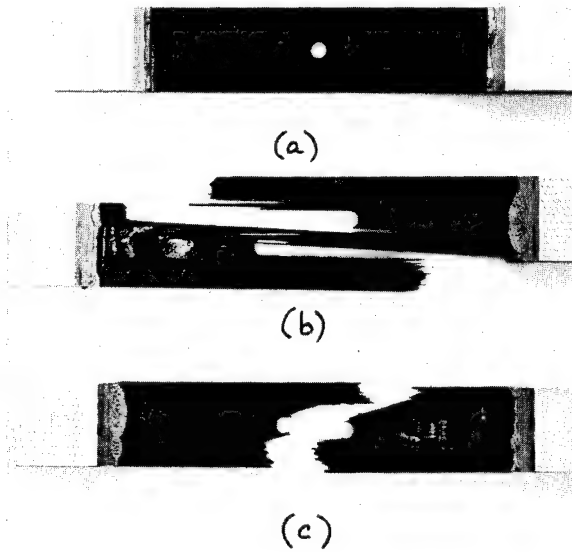


Figure 35. Static Test Specimens:
(a) Fatigue Specimen, (b) A-1-26 (with hole),
(c) B-1-2 (with hole).

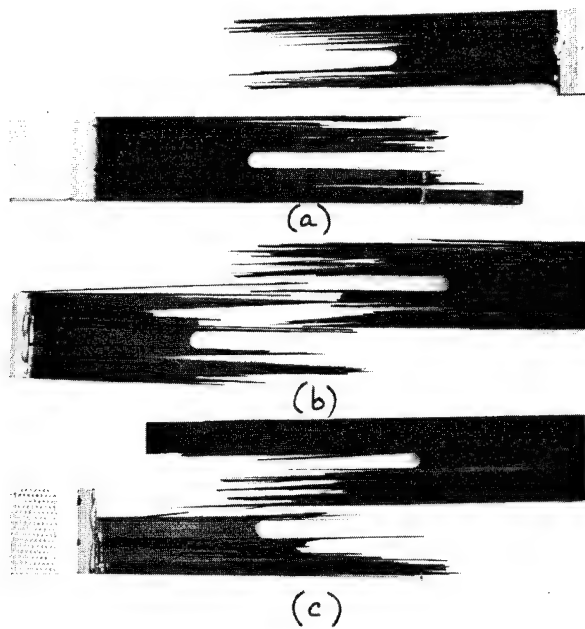


Figure 36. Tensile Fatigue Specimens A (25 Hertz);
 (a) 70% F_{tu} , (b) 62.5% F_{tu} , (c) 55% F_{tu} .

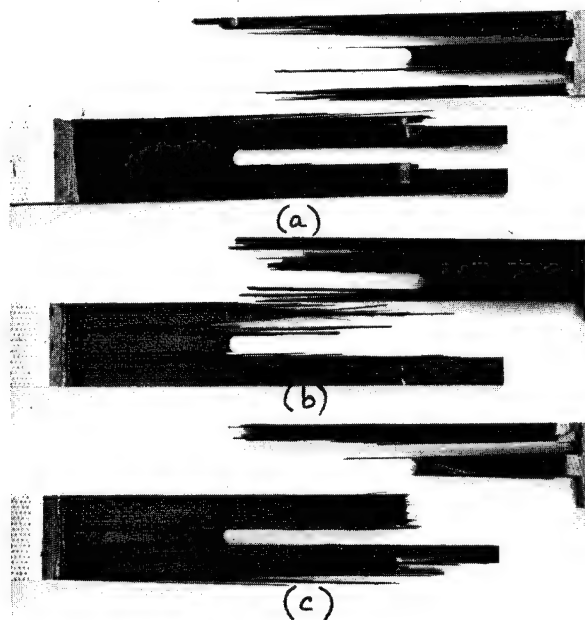


Figure 37. Tensile Fatigue Specimens A (3 Hertz);
 (a) 70% F_{tu} , (b) 62.5% F_{tu} , (c) 55% F_{tu} .

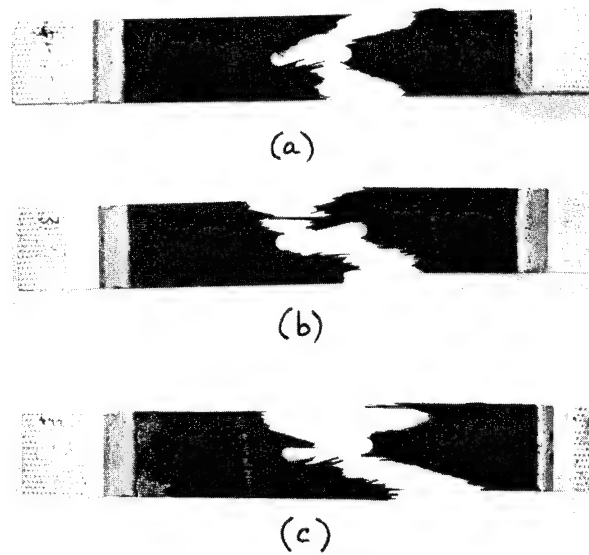


Figure 38. Tensile Fatigue Specimens B (25 Hertz);
 (a) 70% F_{tu} , (b) 62.5% F_{tu} , (c) 55% F_{tu} .

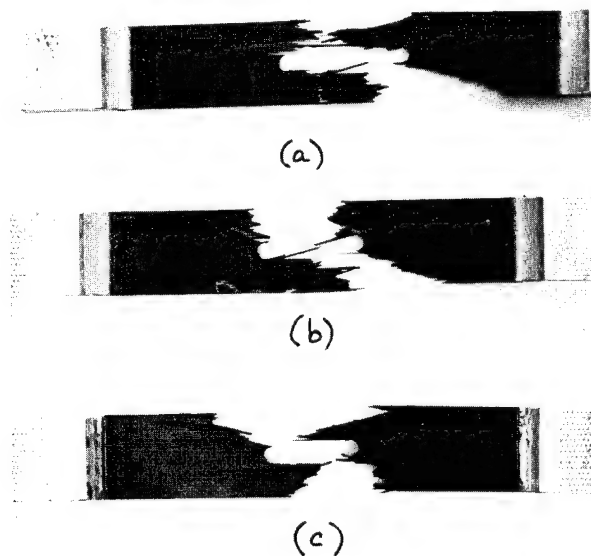


Figure 39. Tensile Fatigue Specimens B (3 Hertz);
 (a) 70% F_{tu} , (b) 62.5% F_{tu} , (c) 55% F_{tu} .

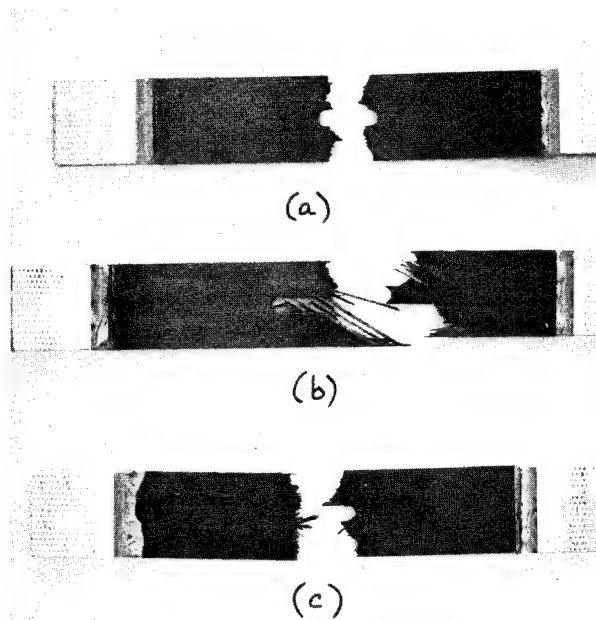


Figure 40. Tensile Fatigue Specimens C (25 Hertz);
 (a) 70% F_{tu} , (b) 62.5% F_{tu} , (c) 55% F_{tu} .

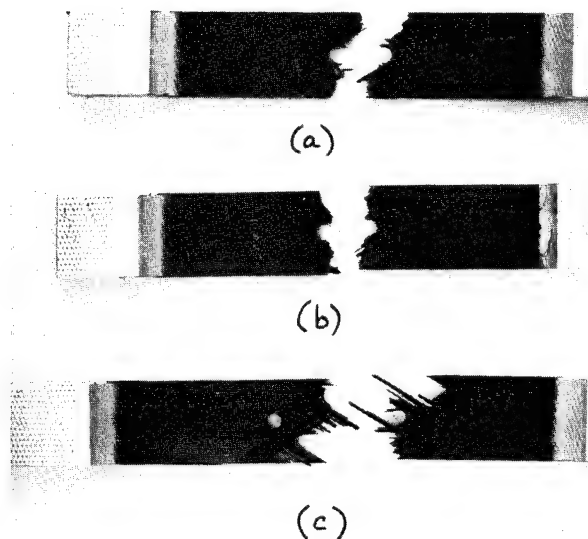


Figure 41. Tensile Fatigue Specimens C (3 Hertz);
 (a) 70% F_{tu} , (b) 62.5% F_{tu} , (c) 55% F_{tu} .

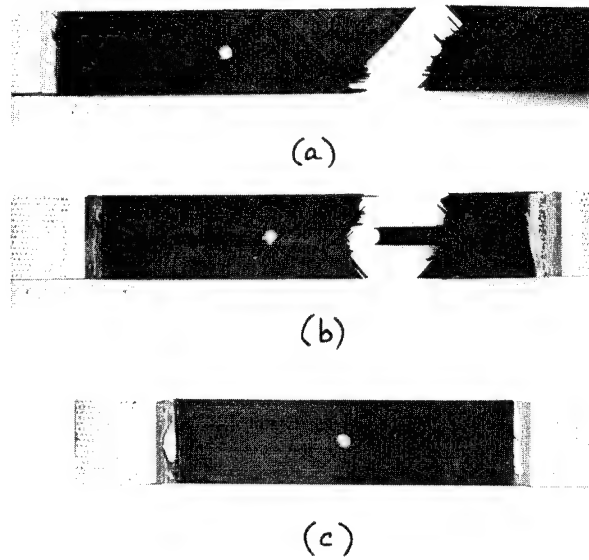


Figure 42. Tensile Fatigue Specimens D (25 Hertz);
 (a) 70% F_{tu} , (b) 62.5% F_{tu} , (c) 55% F_{tu} .

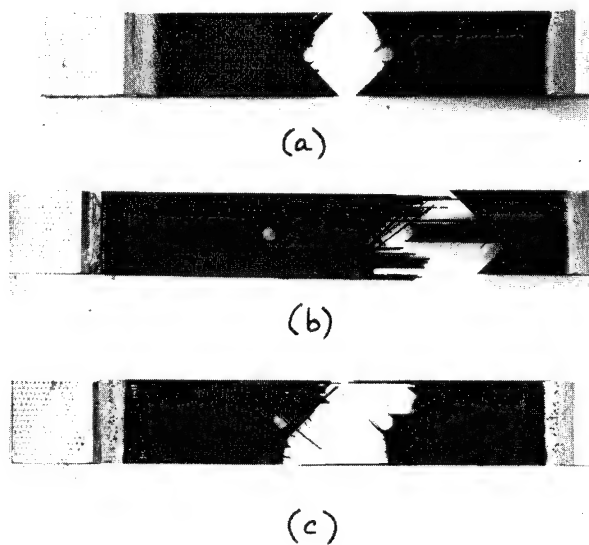


Figure 43. Tensile Fatigue Specimens D (3 Hertz);
 (a) 70% F_{tu} , (b) 62.5% F_{tu} , (c) 55% F_{tu} .

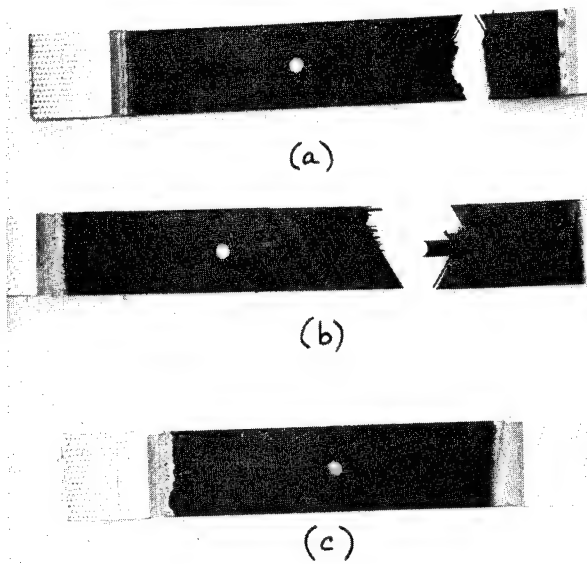


Figure 44. Tensile Fatigue Specimens E (25 Hertz);
 (a) 70% F_{tu} , (b) 62.5% F_{tu} , (c) 55% F_{tu} .

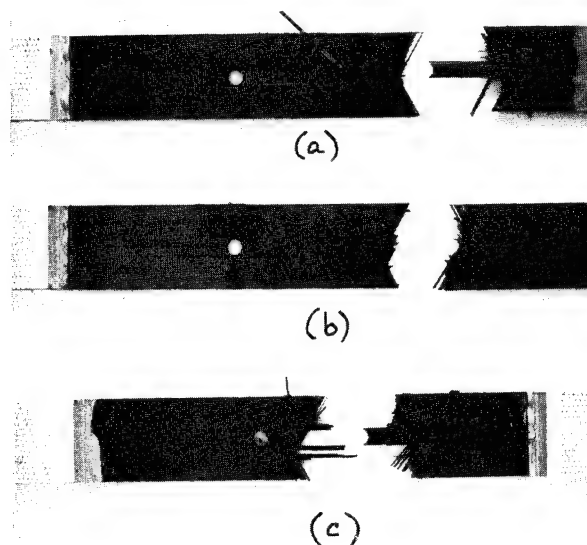


Figure 45. Tensile Fatigue Specimens E (3 Hertz);
 (a) 70% F_{tu} , (b) 62.5% F_{tu} , (c) 55% F_{tu} .

SECTION V

DISCUSSION

The analytical characterization of the load and deformation distributions within a multilayer fiber composite plate, with and without a circular hole, under both static and dynamic loading conditions was initiated. The generalized anisotropic plate analysis for static loading conditions without flaw (circular hole) was developed to derive the field equations and boundary conditions necessary for further analytical development. This generalized anisotropic plate analysis has been reported in various forms in the technical literature.

The field equations derived were used in the analytical development of the dynamic plate model (no hole). The field equations were expressed in finite difference form. A homogeneous set of field equations corresponding to the static case was solved by incrementing time to achieve required boundary displacements and then iterating for the displacement field. The strain energy density fields for both static and dynamic loadings of a unidirectional graphite-epoxy were developed for several initial displacements. The correlation of strain energy density with the strain energy release rate (G) would be a basis for a theory of failure in a future study.

The generalized anisotropic plate analysis produced field equations which were converted into finite difference form in order to develop the static and dynamic plate model with a circular hole. Specification of the boundary conditions at the circular hole was not properly modeled. As a result, the strain energy density fields and stress concentrations around the hole were not calculated.

The Thornel 300/5208 static and tensile fatigue test specimens were provided by the Air Force Flight Dynamics Laboratory. Sendekyj, et al

[32] stated that the tensile modulus of the unidirectional composite was $23\text{--}25 \times 10^6$ psi. This was slightly higher than 21.9×10^6 psi. Also noted were a shear modulus (G) of 0.77×10^6 psi and tensile modulus of 90° fiber oriented composite of 1.6×10^6 psi. The fiber orientations containing $\pm 30^\circ$ and $\pm 45^\circ$ plies demonstrated tensile proportional limits. The other static specimens demonstrate a stiffening effect rather than a proportional limit.

The tensile fatigue data were generated for five fiber orientations, three loading conditions, and two frequencies. The S_{\max} used was 55%, 62.5%, and 70% of tensile ultimate stress determined by static test. The applied stress considered the plate without a circular hole. For all fiber orientations tested at 25 Hertz, the 55% F_{tu} specimen did not fail at 10^6 cycles. For 70% F_{tu} , the specimens failed after a few thousand cycles. Testing at 3 Hertz produced lower fatigue lines. At 70% F_{tu} , failure occurred after a few hundred cycles for all fiber orientations. The 55% F_{tu} specimens failed between 200,000 to 300,000 cycles except $[0/\pm 45/0]_s$ which failed around 450,000 cycles. The low frequency fatigue specimens have lower lives than the high-frequency fatigue specimens. The damage mechanisms occurring within the composites appear to be related to frequency (time) and level of loading. The mechanisms appear to be of a similar type.

The unidirectional (A) Thornel 300/5208 composites failed under maximum strain conditions in static and tensile fatigue loadings. Secondary effects included fiber breakage and pullout from the grips. The degree of fragmentation was related to loading conditions and frequency. The static specimen the least fragmentation, followed by low-cycle then high-cycle fatigue specimens. Static specimen C failed by the $\pm 30^\circ$ plies fracturing causing the 0° plies to fail. The tensile fatigue specimens

failed in a similar manner with the crack originating at the center hole. Static specimen D failed cleanly across the width. Secondary failure effects were noted in the tensile fatigue specimens. These included delamination (due to Poissons effect), fiber breakage, and edge fiber delamination. The crack was initiated at the center hole and propagated between the $+45^\circ$ and the -45° plies longitudinally until fracture occurred. Static specimen E failed in the $+60^\circ$ direction. The tensile fatigue specimens failed similar to the D specimens with the same secondary effects and longitudinal delamination.

This research has outlined several variables which influence the failure of graphite-epoxy composites. The data indicates trends not specifics to establish a definite theory of failure.

SECTION VI

CONCLUSIONS

The analytical characterization of the load and deformation distributions within a multilayer fiber composite plate (without hole) under both static and dynamic loading conditions was accomplished using the finite difference method.

Static and tensile fatigue testing of Thornel 300/5208 composites with and without holes, was accomplished. Tensile fatigue testing involved five fiber orientations, three loading conditions, and two frequencies. Specimens tested at 3 Hertz had lower tensile fatigue properties than those tested at 25 Hertz.

The failure surfaces of the specimens demonstrated the effect of testing conditions. Secondary failure mechanisms such as: delamination, fiber breakage, and edge fiber delamination, were present in D and E specimens. Longitudinal delamination of the D and E specimens was unexpected. The static, low-frequency fatigue, and high frequency fatigue failures were generally similar, differing only in degree.

REFERENCES

1. A.A. Griffith, "The Phenomena of Rupture and Flow in Solids", Phil. Trans. Roy. Soc. London, Vol. A 221 (1920), p. 163.
2. G.R. Irwin, "Analysis of Stresses and Strains Near the End of a Crack Traversing a Plate", J. Applied Mechanics, Vol. 24 (3), (1957), p. 361.
3. G.P. Cherepanov, "Crack Propagation in Continuous Media", J. Applied Mathematics and Mechanics, Vol. 31 (3), (1957), p. 503.
4. B.V. Koxtrov and L.V. Kikitin, "Longitudinal Shear Crack with an Infinitely Narrow Plastic Zone", J. Applied Mathematics and Mechanics, Vol. 31 (3), (1967), p. 334.
5. R.V. Goldshtein, "On Surface Waves in Joined Elastic Materials and their Relation to Crack Propagation Along the Junction", J. Applied Mathematics and Mechanics, Vol. 31 (3), (1967), p. 468.
6. B. Cotterell, "On the Nature of Moving Cracks", J. Applied Mechanics, Vol. 31 (1964), p. 12.
7. I.M. Daniel, "Photoelastic Study of Crack Propagation in Composite Models", J. Composite Materials, Vol. 4 (1970), p. 178.
8. T. Koufopoulos and P.S. Theocaris, "Shrinkage Stresses in Two-Phase Materials", J. Composite Materials, Vol. 3 (1969), p. 308.
9. A.W. Leissa, W.E. Clausen, and G.K. Agrawal, "Stress and Deflection Analysis of Fibrous Composite Materials under External Load-Further Studies", Technical Report, AFML-TR-68-203, 1968.
10. T.F. MacLaughlin, "Effect of Fiber Geometry on Stress in Fiber Reinforced Composite Materials", J. Experimental Mechanics, Vol. 6 (1966), p. 481.
11. P.M. Scop and A.S. Argon, "Statistical Theory of Strength of Laminated Composites", J. Composite Materials, Vol. 2 (1968), p. 82.

12. E. Friedman, "A Tensile Failure Mechanism for Whisker Reinforced Composites", General Electric Publication, Space Sciences Laboratories (no date available), Philadelphia.
13. J.C. Halpin, J.R. Kopf, and W. Goldber, "Time Dependent Static Strength and Reliability for Composites", J. Composite Materials, Vol. 4 (1970), p. 462.
14. R. Hill, The Mathematical Theory of Plasticity, Oxford University Press, London (1950).
15. V.D. Azzi and S.W. Tsai, "Anisotropic Strength of Composites", Experimental Mechanics, Vol. 5 (1965), p. 283.
16. C.C. Chamis, "Failure Criteria for Filamentary Composites", Composite Materials: Testing and Design, ASTM-STP 460, ASTM (1969).
17. S.W. Tsai and E.M. Wu, "A General Theory of Strength for Anisotropic Materials", J. Composite Materials, Vol. 5 (1971), p. 58.
18. E.M. Wu, "Fracture Mechanics of Anisotropic Plates", Composite Materials Workshop, Technomic Publishing Co., (1968).
19. A.S. Tetelman, "Fracture Processes in Fiber Composite Materials", Composite Materials: Testing and Design, ASTM STP 460, ASTM (1969).
20. C. Zweben, "Tensile Strength of Fiber-Reinforced Composites: Basic Concepts and Recent Developments", Composite Materials: Testing and Design, ASTM-STP 460, ASTM (1969).
21. M.E. Waddoups, J.R. Eisenmann, and B.E. Kaminski, "Macroscopic Fracture Mechanics of Advanced Composite Materials", J. Composite Materials, Vol. 5 (1971), p. 446.
22. G.C. Sih, P.D. Hilton, R. Badaliane, P.S. Shenberger and G. Villarreal, "Fracture Mechanics Studies of Composite Systems", Technical Report AFML-TR-70-112, Part II (1971).

23. D.C. Phillips, "The Fracture Mechanics of Carbon Fiber Laminates", J. Composite Materials, Vol. 8 (1974), p. 130
24. M.J. Salkind, "Fatigue of Composites", Composite Materials: Testing and Design, ASTM-STP 497, ASTM (1972).
25. R.D. Holmes and D.W. Wright, "Creep and Fatigue Characteristics of Graphite/Epoxy Composites", ASME Paper No. 70-DE-32 (1970).
26. G.P. Sendeckyj, "A Brief Survey of Empirical Multiaxial Strength Criteria for Composites", Composite Materials: Testing and Design, ASTM-STP 497. ASTM (1972).
27. Z. Haskin and A. Rotem, "A Fatigue Failure Criterion for Fiber Reinforced Materials", J. Composite Materials, Vol. 7 (1973), p. 448.
28. S. Timoshenko and J.N. Goodier, Theory of Elasticity, McGraw-Hill Book Company, Inc., New York (1951).
29. S.W. Tsai, "Strength Characteristics of Composite Materials", NASA-CR-224, (1965).
30. R.C. Reuter, "On the Plate Velocity of a Generally Orthotropic Plate", J. Composite Materials, Vol. 4 (1970), p. 129.
31. "Thornel 300 Graphite Yarn", Technical Bulletin No. 465-223bb, Union Carbide Corporation.
32. G.P. Sendeckyj, M.D. Richardson, and J.E. Pappas, "Fracture Behavior of Thornel 300/5208 Graphite-Epoxy Laminates", Presented at Composite Reliability Conference, Las Vegas, Nevada, April 1974.

FINAL REPORT DISTRIBUTION LIST

	<u>Copies</u>
NASA-Lewis Research Center 21000 Brookpark Rd. Cleveland, OH 44135	
Attn: G. M. Ault, MS 3-5	1
J. C. Freche, MS 49-1	1
C. C. Chamis, MS 49-3	10
R. W. Hall, MS 49-1	1
R. H. Johns, MS 49-3	1
R. H. Kemp, MS 49-3	1
T. T. Serafini, MS 49-1	1
M. P. Hanson, MS 501-7	1
Contracting Officer, MS 500-313	1
National Aeronautics and Space Administration Washington, DC 20546	
Attn: RW/G. C. Deutsch	1
NASA-Langley Research Center Langley Station Hampton, VA 23365	
Attn: M. F. Card	1
R. A. Pride, MS 188A	1
Jet Propulsion Laboratory 4800 Oak Grove Dr. Pasadena, CA 91103	
Attn: A. Knoell, MS 158224	1
Lawrence Livermore Laboratory University of California P. O. Box 808, L-421 Livermore, CA 94550	
Attn: T. T. Chiao	1
Picatinny Arsenal PLASTECH B3401 Dover, NJ 07801	
Attn: H. Heibly	1
U. S. Naval Air Systems Command Code Air-52032D Washington, DC 20360	
Attn: M. Stander	1

U. S. Army Materials and Mechanics Research Center
 Building 39, TAMRL
 Watertown, MA 02072
 Attn: E. M. Leno

1

U. S. Naval Ordnance Laboratory
 White Oak
 Silver Spring, MD 20910
 Attn: F. R. Barnet

1

Wright-Patterson Air Force Base
 Dayton, OH 45433
 Attn: J. Halpin, AFML
 C. D. Wallace, AFFDL/DA
 S. W. Tsai, AFML (MANC)
 G. P. Sendekyj, AFFDL/FBEC
 T. J. Reinhart, AFML/LAE

1

1

1

1

1

University of Dayton
 Research Institute
 KL-565
 Dayton, OH 45409
 Attn: W. S. Blaine

1

Drexel University
 Dept. of M. E. and Mechanics
 32nd and Chestnut
 Philadelphia, PA 19104
 Attn: R. H. Toland

1

IIT Research Institute
 10 West 35th St.
 Chicago, IL 60616
 Attn: I. M. Daniel

1

College of Engineering
 University of Illinois
 Dept. of Theoretical and Applied Mechanics
 Urbana, IL
 Attn: H. I. Corten

1

Illinois Institute of Technology
 10 West 32nd St.
 Chicago, IL 60616
 Attn: L. J. Broutman

1

Massachusetts Institute of Technology
 Dept. of Civil Engineering
 Cambridge, MA 02139
 Attn: F. J. McGarry
 J. F. Mandell

1

1

3

University of Oklahoma
School of Aerospace Mechanics and Nuclear Engineering
Norman, OK 73069
Attn: C. W. Bert

1

Southwest Research Institute
Dept. of Structural Research
8500 Culebra Rd.
San Antonio, TX 78284
Attn: G. C. Grimes

1

Virginia Polytechnic Institute
Dept. of Engineering Mechanics
Blacksburg, VA 24061
Attn: R. A. Heller

1

Washington University
Materials Research Laboratory
St. Louis, MO 63130
Attn: E. M. Wu

1

University of Wyoming
College of Engineering
Dept. of Mechanical Engineering
University Station Box 3295
Laramie, WY 82070
Attn: D. F. Adams

1

Babcock and Wilcox Company
Advanced Composites Department
Box 419
Alliance, OH 44601
Attn: K. Lauraitis

1

Battelle Memorial Institute
Columbus Laboratories
505 King Ave.
Columbis, OH 43201
Attn: B. Noton

1

Boeing Aerospace Company
P. O. Box 3999
Seattle, WA 98124
Attn: J. T. Hoggatt

1

United Aircraft Research Laboratories
East Hartford, CT 06108
Attn: M. A. DeCrescente (High Temp. Mat'ls. Dept.)

1

E. I. DuPont
Experimental Station
Building 262
Wilmington, DE 19892
Attn: C. Zweben

1

General Electric Company
Materials and Processes Technology Laboratory
Evendale, OH 45215
Attn: R. Ravenhall

1

General Dynamics Corporation
Ft. Worth, TX 76101
Attn: M. E. Waddoups

1

General Dynamics
Convair Division
P. O. Box 1128
San Diego, CA 92112
Attn: J. E. Ashton

1

Goldsworthy Engineering, Inc.,
2917 Lomita Blvd.
Torrance, CA 90505
Attn: B. H. Jones

1

Douglas Aircraft Company
Cl-250, 35/41
3855 Lakewood Blvd.
Long Beach, CA 90801
Attn: S. Y. Elliott

1

Grumman Aerospace Corporation
Bethpage, NY 11714
Attn: R. N. Hadcock

1

Hercules Incorporated
Allegheny Ballistic Laboratory
Cumberland, MD 21502
Attn: A. A. Vicario

1

Hughes Aircraft Company
Space and Communications Group
Technology Division
El Segundo, CA
Attn: P. W. Bernstein

1

McDonnell Douglas Astronautics Company
A3-250, MS 13-2
5301 Bolsa Ave.
Huntington Beach, CA 92647
Attn: L. B. Greszczuk

1

Martin-Marietta Corporation
Denver, CO
Attn: A. Holston

1

Materials Sciences Corporation
P. O. Box 254
Ft. Washington, PA 19034
Attn: B. W. Rosen

1

National Bureau of Standards
Engineering Mechanics Section
Washington, DC 20234
Attn: R. Mitchell

1

North American Rockwell
International Airport
Los Angeles Division
Los Angeles, CA 90009
Attn: L. M. Lackman

1

Sikorsky Aircraft
Division of UAC
Stratford, CT 06602
Attn: M. J. Salkind

1

Whittaker Corporation
Research and Development
3540 Aero Court
San Diego, CA 92123
Attn: R. K. Berg

1